Geoelectrical Measurement of Multi-Scale Mass Transfer Parameters

Final Report to the Subsurface Biogeochemical Research Program

Grant # DE-SC0002007

Project Duration: September 1, 2009 – August 31, 2012 (original)

Project Manager: David Lesmes

Frederick D. Day-Lewis, US Geological Survey, Branch of Geophysics, 11 Sherman Place, Unit 5015, Storrs CT 06269; ph. 860.487.7402 x21

Kamini Singha (co-PI), Hydrologic Science and Engineering, Colorado School of Mines, 1516 Illinois St., Golden, CO 80401; ph.: 303.273.3822; email: ksingha@mines.edu

Roy Haggerty (co-PI), Dept. of Geosciences, 104 Wilkinson Hall, Oregon State U., Corvallis, OR 97331; ph.: 541.737.1210; email: haggertr@geo.oregonstate.edu

Timothy C. Johnson (co-PI), Pacific Northwest National Laboratory, Pacific Northwest National Laboratory, 902 Battelle Blvd., Richland WA, 99352, USA, TJ@pnnl.gov

Andrew Binley (co-PI), Lancaster Environment Centre, Lancaster U., Bailrigg, Lancaster, LA1 4YQ, UK; ph. +44 1524 593927; email: a.binley@lancaster.ac.uk

John W. Lane, Jr. (co-PI), US Geological Survey, Branch of Geophysics, 11 Sherman Place, Unit 5015, Storrs CT 06269; ph. 860.487.7402 x13

Project Summary

Mass transfer affects contaminant transport and is thought to control the efficiency of aquifer remediation at a number of sites within the Department of Energy (DOE) complex. An improved understanding of mass transfer is critical to meeting the enormous scientific and engineering challenges currently facing DOE. Informed design of site remedies and long-term stewardship of radionuclide-contaminated sites will require new cost-effective laboratory and field techniques to measure the parameters controlling mass transfer spatially and across a range of scales. In this project, we sought to capitalize on the geophysical signatures of mass transfer. Previous numerical modeling and pilot-scale field experiments suggested that mass transfer produces a geoelectrical signature—a hysteretic relation between sampled (mobile-domain) fluid conductivity and bulk (mobile + immobile) conductivity—over a range of scales relevant to aquifer remediation. In this work, we investigated the geoelectrical signature of mass transfer during tracer transport in a series of controlled experiments to determine the operation of controlling parameters, and also investigated the use of complex-resistivity (CR) as a means of

quantifying mass transfer parameters in situ without tracer experiments. In an add-on component to our grant, we additionally considered nuclear magnetic resonance (NMR) to help parse mobile from immobile porosities. Including the NMR component, our revised study objectives were to:

1. *Develop and demonstrate geophysical approaches to measure mass-transfer parameters spatially and over a range of scales, including the combination of electrical resistivity monitoring, tracer tests, complex resistivity, nuclear magnetic resonance, and materials characterization; and*
2. *Provide mass-transfer estimates for improved understanding of contaminant fate and transport at DOE sites, such as uranium transport at the Hanford 300 Area.*

To achieve our objectives, we implemented a 3-part research plan involving (1) development of computer codes and techniques to estimate mass-transfer parameters from time-lapse electrical data; (2) bench-scale experiments on synthetic materials and materials from cores from the Hanford 300 Area; and (3) field demonstration experiments at the DOE's Hanford 300 Area. In a synergistic add-on to our workplan, we analyzed data from field experiments performed at the DOE Naturita Site under a separate DOE SBR grant, on which PI Day-Lewis served as co-PI. Techniques developed for application to Hanford datasets also were applied to data from Naturita.

1. Introduction

The Department of Energy (DOE) faces enormous scientific and engineering challenges associated with the remediation of legacy contamination at former nuclear weapons production facilities. Selection, design and optimization of appropriate site remedies (e.g., pump-and-treat, biostimulation, or monitored natural attenuation) requires reliable predictive models of radionuclide fate and transport; however, our current modeling capabilities are limited by an incomplete understanding of multi-scale mass transfer—its rates, scales, and the heterogeneity of controlling parameters. At many DOE sites, long "tailing" behavior, concentration rebound, and slower-than-expected cleanup are observed; these observations are all consistent with multi-scale[1] mass transfer [*Haggerty and Gorelick*, 1995; *Haggerty et al.*, 2000; 2004], which renders pump-and-treat remediation and biotransformation inefficient and slow [*NRC*, 1992; *Haggerty and Gorelick*, 1994; *Harvey et al.*, 1994; *Wilson*, 1997]. Despite the importance of mass transfer, there are significant uncertainties associated with controlling parameters, and the prevalence of mass transfer remains a point of debate [e.g., *Hill and Barlebo*, 2006; *Molz et al*., 2006] for lack of experimental methods to verify and measure it in situ or independently of tracer breakthrough.

There is a critical need for new field-experimental techniques to measure mass transfer in-situ and estimate multi-scale and spatially variable mass-transfer parameters. The current lack of such techniques results in large parameter uncertainty, which in turn translates into enormous prediction uncertainty and cost to DOE. In this project, we considered three hydrogeophysical

[1] This is more commonly referred to as "multirate" mass transfer; however, to be consistent with terminology currently used at the DOE's Hanford 300A Integrated Field Challenge (IFC) project, we will adopt the term "multi-scale," which could imply scales in both time and space.

approaches for providing information about mass-transfer parameters: (1) the combination of electrical-resistivity tomography (ERT) and ionic tracer experiments to explore rates of exchange and relative mobile and immobile porosities; (2) complex resistivity (CR) measurements to infer the distribution of diffusive length scales active in a porous medium; and (3) nuclear magnetic resonance (NMR) to estimate mobile and immobile porosity.

2. Project Objectives

Our study objectives were to:

1. *Develop and demonstrate geophysical approaches to measure mass-transfer parameters spatially and over a range of scales, including the combination of electrical resistivity monitoring, tracer tests, complex resistivity, nuclear magnetic resonance, and materials characterization; and*

2. *Provide mass-transfer estimates for improved understanding of contaminant fate and transport at DOE sites, such as uranium transport at the Hanford 300 Area.*

3. Background

We briefly review the science of mass transfer and the basis for electrical measurement of controlling parameters underlying our three measurement approaches: (1) time-lapse ERT combined with ionic tracer tests; (2) CR; and (3) NMR. In the first approach, ERT imaging and conventional chemical sampling are used to monitor the exchange of solute between mobile and immobile domains and infer mass-transfer parameters from model calibration. In the second, measurements of CR are used, in the absence of any tracer, to characterize the distribution of diffusive length scales present in a porous medium. In the third, NMR is used to estimate pore-size distribution and segregate pore space into mobile and immobile porosity, also in the absence of tracers.

3.1 Mass Transfer

Mass transfer has been used to explain tailing—the progressively slower recovery of concentration through time—and contaminant rebound in fractured and heterogeneous porous media [e.g., *Goltz and Roberts*, 1986; *Wood et al.*, 2000; *Haggerty and Gorelick*, 1995; *Feehley et al.*, 2000; *Haggerty et al.*, 2000; *Harvey and Gorelick*, 2000; *Haggerty et al.*, 2001; *McKenna et al.*, 2001; *Dentz and Berkowitz*, 2003]. In models of multi-scale mass transfer, an aquifer is conceptualized as consisting of multiple, overlapping continua between which mass exchanges through diffusion. In the simplest conceptualization—the first-order mobile-immobile domain model—a representative elementary volume (**Figure 1**) is a bicontinuum consisting of (1) well-connected pore space (mobile domain), and (2) poorly connected pore space (immobile domain). Advection and dispersion occur in the mobile domain with exchange between domains modeled by the general mass transfer ADE [*Haggerty et al.*, 2000]:

$$\theta_m \frac{\partial c_m}{\partial t} + \theta_{im} \frac{\partial}{\partial t} \int_0^t c_m(t-\tau) g_*(\tau) d\tau = \nabla \cdot (\theta_m D \nabla c_m) - \theta_m v \cdot \nabla c_m , \quad (1)$$

where c_m is the concentration in the mobile domain, D is the hydrodynamic dispersion tensor, v is the pore water velocity vector, θ_m is the porosity of the mobile domain, θ_{im} is the porosity of the immobile domain, t is time, and $g_*(\tau)$ is a memory function that relates the rate of return of mass to the mobile domain based on the mass that went into the immobile domain at τ earlier time [*Haggerty et al.*, 2000 modified from *Carrera et al.*, 1998]. Concentration in the immobile domain can be calculated from c_m and $g_*(t)$. Linear exchange with a single time-scale of transfer is often assumed, in which case **Eq. 1** can be simplified to the conventional mobile-immobile domain model by setting $g_*(t) = \alpha e^{-\alpha t}$ [e.g., as used by *Singha et al.*, 2007, where α is a first-order rate coefficient]. More sophisticated mass transfer models are also possible, e.g., models involving multiple rates or diffusion into/from spheres [*Haggerty and Gorelick*, 1995] or all of these and sorption [*Cunningham et al.*, 1997]. Mass transfer is thought to occur over a wide range of scales from the microscopic (e.g., in and out of grains), to the mesoscopic (e.g., fractures), to the macroscopic (e.g., aquifer facies) [e.g., *Harvey and Gorelick*, 2000; *Feehley et al.*, 2000; *Haggerty et al.*, 2004]. Distributions of transfer rates associated with multiple scales of heterogeneity have been represented with multi-rate models, in which rates follow statistical distributions, such as the lognormal [*Haggerty and Gorelick*, 1998], gamma [*Culver et al.*, 1997; *Werth et al.*, 1997], or power-law [*Haggerty et al.*, 2000; *Schumer et al.*, 2003], which can be handled by choice of $g_*(\tau)$. Still other forms of $g_*(\tau)$ provide other models of the immobile-domain residence time (e.g., matrix diffusion). *Dentz and Berkowitz* [2003] and *Berkowitz et al.* [2006] showed that **Eq. 1** is equivalent to the long-time limit of the continuous time random walk if particle motions are assumed Gaussian and independent in time[2]. *Schumer et al.* [2003] showed that the fractional-in-time advection-dispersion equation (time-fADE) is a subset of **Eq. 1**.

There is a crucial lack of approaches to inform parameterization of mass-transfer models independently of tracer breakthroughs. Even with extensive, expensive and destructive coring, it is not possible to sample all scales of heterogeneity present in the field, and insight into immobile-domain concentration and transfer between mobile and immobile domains remains problematic. Although mass-transfer models have successfully matched field data [e.g., *Feehley et al.*, 2000; *Harvey and Gorelick*, 2000], their validity and utility are debated [*Hill et al.*, 2006; *Molz et al.*, 2006]. Experimental verification of mass transfer in field settings is difficult because conventional geochemical measurements preferentially sample pore fluid from the mobile domain and provide only indirect information about concentration of the immobile domain; hence, only circumstantial evidence is available to verify mass transfer or identify values of controlling parameters.

[2] It is important to note that the *spatial*-fADE is not equivalent to the model given here and that while less common in the literature to date, the CTRW can employ particle motion distributions that are non-Gaussian and correlated in time.

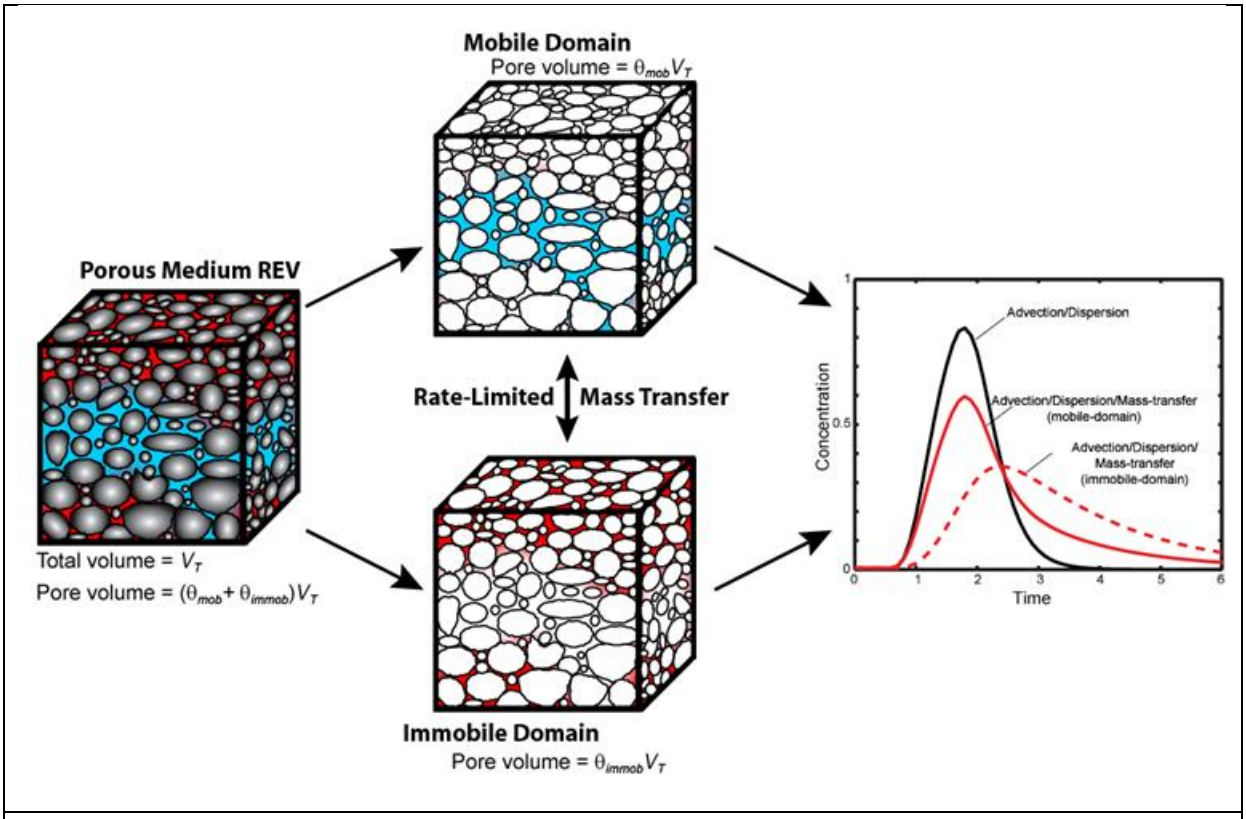

Figure 1. Conceptual model of mass transfer. A representative elementary volume (REV) is consists of multiple domains (two shown here). Advection and dispersion occur in the mobile domain, which consists of the open, connected pore space and/or fractures. Exchange between the mobile domain and immobile domain, which consists of poorly connected pores or dead-end fractures, is modeled as a diffusive process. The rate(s) of diffusion are controlled by the distribution of length scales—possibly from the grain to facies scales.

3.2. Basis for Electrical-Resistivity Tomography Monitoring of Mass Transfer

Electrical and electromagnetic geophysical methods have long been used to characterize and monitor pore-fluid salinity and total dissolved solids (TDS), based on petrophysical relations between bulk and fluid resistivity. For example, assuming Archie's Law, changes in fluid resistivity manifest changes in bulk electrical resistivity according to:

$$\Delta\rho_b = F \cdot \Delta\rho_f \tag{2}$$

where ρ_f is the change in fluid resistivity from the background as measured in the field, ρ_b is the change in bulk resistivity from the background, and F is the formation factor. The formation factor has been defined in various ways [*Wyllie and Rose*, 1950; *Archie*, 1952; *Winsauer et al.*, 1952] but was originally conceived as a function of porosity and cementation [*Guyod*, 1944]. Empirical relations are available to relate TDS to fluid resistivity [e.g., *Keller and Frischknecht*,

1966]. In the presence of clays and surface conduction, alternative models are available for **Eq. 2**, e.g., Waxman-Smits [*Waxman and Smits*, 1968] and *Hanai-Bruggeman* [*Bussian*, 1983].

Eq. 2 (and similar models that address surface-conduction) provide the basis for ERT monitoring ionic content of fluids in the pore space at the sub-meter to 10s-of-meters scale. Recent advances in hydrogeophysical technology and data analysis are enabling aquifer characterization and monitoring of hydrologic processes at spatial and temporal resolution heretofore impossible [*Rubin and Hubbard*, 2005; *Vereecken et al.*, 2006]. Time-lapse geophysical imaging has provided high-resolution (in space and time) information about transport of fluids and solutes in diverse geologic settings. Geoelectrical and radar methods have been used extensively to monitor subsurface transport of conductive tracers in the lab [*Ward et al., 1995*; *Binley et al.*, 1996; *Slater et al*., 2000, 2002] and field [*Kemna et al.*, 2002; *Day-Lewis et al.*, 2003, 2006; *Singha and Gorelick*, 2005; 2006].

In the presence of mass transfer, non-equilibrium between mobile and immobile concentrations would cause the relation between bulk and fluid conductivity to deviate from **Eq. 2** and change over time. For example, consider a push-pull tracer test with an ionic tracer. During the injection, changes in bulk conductivity will lag behind changes in fluid conductivity, because the immobile pore space will have low concentration relative to the mobile domain. Conversely, during the extraction, the immobile domain will have higher concentration, as the tracer is more quickly extracted from the mobile domain and slowly diffuses out of the immobile. During a phase of quiescent storage (interim between injection and extraction), bulk conductivity would remain approximately constant while measured fluid concentration (and conductivity) drops with local diffusive exchange between mobile and immobile domains.

In a bicontinuum model, bulk resistivity can be modeled as [after *Singha et al.*, 2007]:

$$\rho_b = \left(\theta_m + \theta_{im}\right)^{1-m} \left(\theta_m / \rho_{f,m} + \theta_{im} / \rho_{f,im}\right)^{-1}, \tag{3}$$

where $\rho_{f,m}$ is the mobile-domain fluid resistivity at a given location, $\rho_{f,im}$ is the immobile-domain resistivity, θ_m is the mobile domain porosity [-], θ_{im} is the immobile porosity [-], and m is the empirical cementation factor in Archie's Law [*Archie*, 1942]. In the presence of surface conduction (as expected at Hanford), it is a simple matter to substitute the Waxman-Smits or Hanai-Bruggeman models in **Eq. 3**. Combining the transport equation (**Eq. 1**) and bicontinuum petrophysical relation (**Eq. 3**) provides the basis for ERT monitoring of mass transfer.

The combination of ERT and ionic tracer tests has potential to map spatially variable mass-transfer parameters. Application at the lab and field scales may also provide new insights into the scale-dependency of these parameters. Preliminary modeling and pilot-scale experiments confirm the viability of the approach; however, we note two important limitations. First, the scales (or rates) of mass transfer that can be characterized are limited by the ability of ERT to resolve breakthrough curve tails, i.e., small changes in TDS. Second, the use of an ionic tracer is problematic at some sites, where changes in ionic strength may produce unfavorable geochemical reactions. Therefore, we also propose a second strategy free of these limitations.

3.3. Complex Resistivity (CR) Measurements

For frequency-domain geoelectrical measurements made at low frequencies (<1000 Hz), a phase shift exists between injected current and measured voltage. This polarization effect can be described in terms of complex electrical resistivity, ρ^*, or electrical conductivity, σ^*:

$$\sigma^*(\omega) = 1/\rho^*(\omega) = \sigma'(\omega) + i\sigma''(\omega), \quad (4)$$

where σ' and σ'' are the measured real and imaginary components of electrical conductivity, respectively, ω is the excitation frequency and $i = \sqrt{-1}$. The real part of σ^* represents the total energy loss (conduction) whereas the imaginary part represents the total storage loss (polarization). The mechanisms of charge storage vary with excitation frequency [see *Olhoeft*, 1985]. In the low frequency range the overwhelming mechanism is the polarization of the ionic charge associated with the electrical double layer that exists at the mineral-fluid interface due to the pH dependent surface charge on mineral grains.

Previous work shows that the magnitude of this polarization at a single measurement frequency (i.e., σ'') is closely related to microgeometrical properties. It is primarily controlled by the total mineral-fluid surface area within the sample, which can be estimated from the total mineral surface area per unit pore volume (S_{por}). Previous work has shown σ'' to exhibit a near linear dependence on S_{por} [*Börner and Schön*, 1991; *Börner et al.*, 1996; *Slater and Glaser*, 2003]. As grain size and surface are inversely related, other workers have found a near-inverse linear relation between σ'' and effective grain size [*Vanhala*, 1997; *Slater and Lesmes*, 2002] although the exact nature of this relationship depends on how the surface area is distributed across the range of grain sizes [*Slater and Glaser*, 2003]. Fluid chemistry and saturation also influence the polarization and may complicate interpretation of microgeometrical properties [*Klein and Sill*, 1982; *Vinegar and Waxman*, 1984; *Ulrich and Slater*, 2004; *Titov et al.*, 2004].

Important microgeometrical information is also potentially obtainable by analyzing the nature of the frequency dependence of $\sigma^*(\omega)$. This results from the fact that the relaxation time is related to the length-scale of the induced charge separation along the mineral-fluid interface. In studies of UK sandstones, *Scott and Barker* [2003] and *Binley et al* [2005] demonstrated a convincing correlation between a "dominant pore-throat" diameter and the frequency at which a peak in the phase angle occurs. These studies support the hypothesized link between electrical relaxation and some hydraulic length scale in porous media.

The relaxation time of electrical polarization in principle should be inversely related to some measure of diffusion along the grain/fluid boundary [*Lesmes and Friedman*, 2005]. In natural porous media the distribution of diffusion length scales will be apparent from the frequency dependence of the complex resistivity (a distribution of relaxation processes). This link between length scales and electrical behavior has been exploited by researchers seeking

petrophysical models for hydrogeological investigations. In this work, we sought to extract information about the diffusion process itself from the measured complex resistivity.

3.4. Nuclear Magnetic Resonance (NMR) Measurements

Low-field proton NMR measurements can be used to partition the total porosity into θ_m and θ_{im} based on the distribution of transverse relaxation times. The measured NMR signal, $I(t)$, is described by a multiexponential decay

$$I(t) = I_0 \sum_i f_i e^{-t/T_{2i}}, \tag{5}$$

where I_0 is the initial signal magnitude. Using an instrument specific calibration factor, I_0 can be converted into the total volume of water measured in the NMR experiment. The subscript i in **Eq. 5** represents each pore environment and f_i is the fraction of protons relaxing with a relaxation time of T_{2i}. The values of f_i versus T_{2i} are often plotted to show the distribution of relaxation times. In the case of fast diffusion, which assumes that all protons travel to and relax at the solid surface in the time interval of the NMR experiment, the i^{th} relaxation time value is given by [*Brownstein and Tarr*, 1979; *Senturia and Robinson*, 1970]:

$$1/T_{2i} \sim \rho_{2i}/a_i \tag{6}$$

where a_i is the characteristic length scale of the i^{th} water-filled pore, typically described by the inverse of the surface-area-to-volume ratio of the corresponding pore, and ρ_{2i} is the surface relaxivity or the ability of the surface to enhance relaxation. For porous material with uniform ρ_{2i}, e.g. clean sand, the T_2-distribution can be used to represent the pore size distribution. Previous studies have verified this relation for a range of water-saturated porous material including: sandstone and carbonate cores [*Arns*, 2004; *Straley et al.*, 1997]; silica gels [*Valckenborg et al.*, 2001]; fused glass beads [*Straley et al.*, 1987]; and unconsolidated sand and glass beads [*Bird et al.*, 2005; *Hinedi et al.*, 1993]. Furthermore, an early study by *Timur* [1969] showed that θ_{im} can be estimated from $\theta_{im} = \sum_{T_{2i}<T_{2cuttoff}} f_i$, where $T_{2cuttoff}$ is an empirically defined cut-off time; similarly, θ_m can be estimated from $\theta_m = \sum_{T_{2i}>T_{2cuttoff}} f_i$. In sandstone cores, a cut-off time of 33 ms is commonly used to accurately determine θ_m and θ_{im} [*Allen et al.*, 2000; *Timur*, 1969].

NMR measurements of relaxation time distributions in saturated porous media provide approximate estimates of pore size and porosity distributions. However, translation of NMR measurements to transport parameters (i.e., θ_{im} and θ_m) has not been fully demonstrated and validated. NMR relies on using empirical cutoff times, usually of 3 and 33 ms, to split the NMR relaxation time distribution into the volume of clay- or capillary-bound or producible fluids [*Allen et al.*, 2000; *Timur*, 1969]. Large intragranular pores associated with larger NMR relaxation times are expected to be active in advective transport and contribute to θ_m. Smaller intragranular pores associated with smaller NMR relaxation time scales may play negligible role in advective transport and contribute to θ_{im}.

4. Project Performance Sites—The Hanford 300 Area and Naturita UMTRA Site

The Hanford 300 Area is located on the western bank of the Columbia River just north of the town of Richland, WA and covers an area of ~4 km^2. The 300 Area was the location of an interdisciplinary DOE-funded Integrated Field Research Challenge (IFRC) effort focused on multi-scale mass transfer processes. Mass transfer was studied across scales ranging from the grain/pore- up to the sub-watershed. The 300 Area therefore represented the ideal field laboratory for our proposed research, although major logistical challenges related to conducting tracer tests and monitoring with ERT led us to revise our field plans and conduct additional experiments at a second DOE site in Naturita, CO.

4.1. Radionuclide Contamination and Site History at Hanford

Operations in the 300 Area began in 1943 and comprised activities including reactor fuel fabrication and pilot scale evaluation of separation processes. For more than 40 years radiologically and chemically contaminated liquid wastes were disposed by means of sewer lines to unlined infiltration ponds, trenches, and cribs [*Riley et al.*, 1992; *Serne et al.*, 2002]. Uranium is the contaminant of greatest concern in the 300 Area with an estimated minimum 124 tons U disposed at the site in the North and South Process Ponds alone, along with 266 tons of copper, 129 tons of fluorine and 2271 tons of nitrates. In 1993, a uranium transport simulation predicted that U concentrations would decrease to meet the drinking water standard (30 μg/L) within 3 to 10 years. Based on this simulation, an interim record of decision for site remediation was adopted calling for monitored natural attenuation while sources were removed and natural flushing removed remaining U. Despite excavation of the contaminant sources, concentrations in the groundwater have not diminished significantly [*Hartman et al.*, 2006] highlighting a significant knowledge gap in the understanding of U reactive transport upon which the earlier conceptual and numerical models were built.

4.2 Site Geology and Hydrology at Hanford

The unconfined aquifer at the Hanford 300 site is composed of the Hanford (U1) and Ringold E/B gravel formations. The Hanford formation is an informal name for a series of late Pleistocene cataclysmic flood deposits, approximately 15 m thick and dominated by a gravel-rich facies in the 300 area [*Lindberg and Chou*, 2001]. Bulk analysis of the Hanford formation sediments indicates that they are primarily quartz (33-35%) and feldspar (mostly plagioclase [25-34%]) with minor amounts of mica (11-15%), chlorite (3-5%), amphibole (3-5%), and calcite. The clay fraction of the sediments is dominated by smectite (45.71%), with smaller amounts of illite (35.71%), chlorite (10.50%), and kaolinite (8.04%). At the north end of the site (North Process Pond), the Hanford formation extends to the surface suggesting little or no disturbance. Below the zone of disturbance is a crudely stratified bed of clast-supported muddy sandy gravel to muddy gravel with minor lenses of gravelly sand. To the south (South Process Pond),

sediments beyond the disturbed 1.5 m are crudely stratified beds of clast-supported muddy sandy gravel to muddy gravel with minor lenses of gravelly sand. The uranium plume exists largely in the Hanford (U1) formation, which is highly permeable but has some interbedded silt lenses. The Ringold formation is a fluvial formation that underlies the Hanford formation and contains gravel-dominated channel deposits, silt-dominated overbank deposits, and clay-dominated lacustrine deposits totaling approximately 37 meters in thickness [*Lindberg and Chou*, 2001]. The bottom 17 meters of the Ringold formation are clay-dominated lacustrine deposits and create a confining layer for the aquifers 10 below. At the Hanford 300 Area field site, the uppermost aquifer is at about 10 m and is in hydraulic continuity with the Columbia River.

Vadose zone pore water samples show large variations in dissolved U because of spatial heterogeneity in (1) sorbed U(VI), (2) pore-scale desorption/ mass transfer rates, and (3) unsaturated water flow field. Mass-transfer limited desorption is likely a critical U(VI) resupply mechanism to groundwater as the water table fluctuates. Evidence of this mass transfer was demonstrated by *Lui et al.* [2006] with column experiments in which flow interruption was used to study the release of U(VI) from whole (unsieved) sediments collected from the north process pond. Flow interruption involves inhibiting the steady-state flow process during an experiment from a designated period of time, thereby eliminating hydraulic non-equilibrium, and allowing a new physical or chemical equilibrium state to be approached [*Jardine et al.*, 1998].

4.3. Second Project Site: Naturita UMTRA Site, Naturita, CO

The field experiments were conducted at a former uranium mill site located along the San Miguel River in southwestern Colorado, approximately 3 km northwest of the town of Naturita (**Figure 2**). The aquifer is recharged by the river at the southeast end of the site, and discharges back into the river along the northern end [*Curtis et al.*, 2006], creating long flowpaths of groundwater/surface water exchange. Uranium contamination occurs in the shallow, unconfined aquifer at the site; the aquifer is composed of sand, gravel, and cobbles, with mineralogy consisting of quartz and lesser amounts of detrital feldspars, carbonates, magnetite, and fine clay-size materials [*Davis et al.*, 2004; *Curtis et al.*, 2006]. The aquifer is underlain by the Brushy Basin Member, a fine-grained shale approximately 30-m thick. The tracer tests were conducted downgradient of the maximum observed uranium concentrations observed at the site. The depth to water and saturated thickness of the aquifer varies seasonally, and was approximately 3.4 m and 1.6 m, respectively, at the time of the field investigation. Additional details of the overall site characteristics are presented elsewhere [*Davis et al.*, 2004, 2006; *Kohler et al.*, 2004; *Brosten et al.*, 2011], as is a description of an earlier experiment on uranium transport that was conducted at the tracer test site [*Curtis and Davis*, 2006]. The uranium mill was in operation from the 1930's until its closure in 1963. Remediation efforts included removal of contaminated soil from the southern two thirds of the site between 1996 and 1998. The site has been the focus of USGS research on reactive transport of uranium (VI) for over ten years [*Curtis et al.*, 2004, 2006; *Davis et al.*, 2004; *Kohler et al.*, 2004]. Several well clusters were installed for previous research efforts at the site. For our experiments, a new cluster (**Figure 2**) was installed with wells designed for dual-purpose fluid-sampling and geoelectrical monitoring**.**

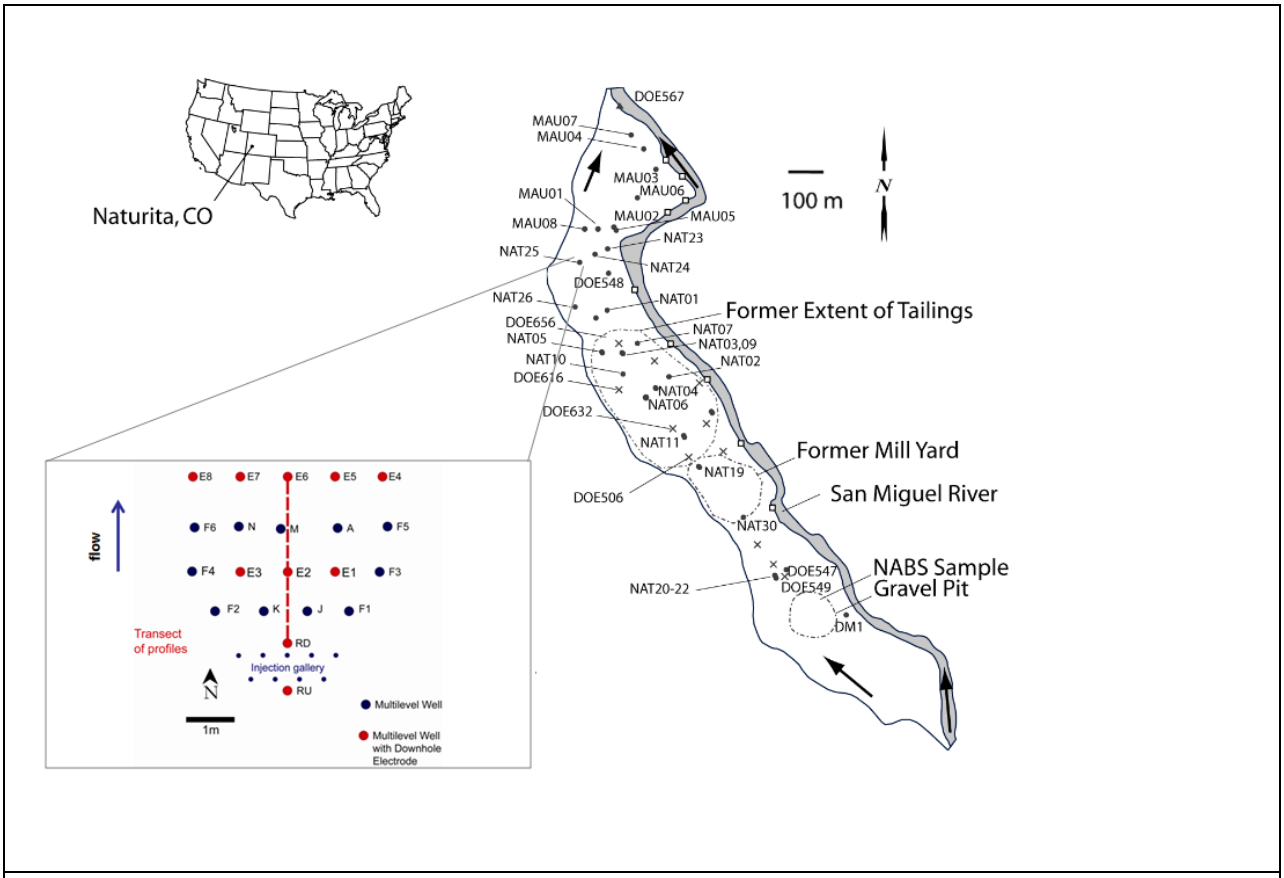

Figure 2. Map of the United States Department of Energy Uranium Mill Tailings Remedial Action site near Naturita, CO, showing the locations of the former mill, ore tailing and monitoring wells. The layout of the tracer site used for this study is depicted in the inset.

5. Approach

Our work comprised a 3-task work plan, which includes method development and modeling; laboratory ERT/tracer, CR and NMR experiments on both synthetic material and material from Hanford; and field experiments in the Hanford 300 Area. NMR measurements were an add-on component to our original plan. Work conducted under this project was also synergistic with a related SBR grant for work at the DOE Naturita site, described here.

5.1. Task 1. Numerical and Analytical Modeling & Tool Development

To jointly analyze time-lapse ERT data and tracer data, we developed codes to (1) perform parametric sweeps over ranges of mass-transfer parameters and evaluate parameter sensitivity for laboratory data [Swanson et al., 2012; in review]; (2) link the solute-transport code MT3DMS [Zheng and Wang, 1999] and the parameter-estimation code UCODE_2005 [Poeter et al., 2005] for analysis of field data [Briggs et al., 2013]; and (3) perform pore-scale simulations

of flow, transport, and electrical conduction in pipe-lattice networks [Day-Lewis et al., in prep]. In addition, in order to analyze CR spectra we developed (with additional support from National Science Foundation grant EAR-0711053) a means of decomposing CR spectra into a distribution of Debye relaxations using a Monte Carlo Markov Chain (MCMC) based approach, as reported in *Keery et al.* [2012].

We additionally developed a method for pore-scale simulation of the electrical signature of mass transfer. In previous work and work performed under this grant, a bicontinuum formulation of Archie's Law was assumed. This model has been shown to be qualitatively consistent with limited field-experimental data; however, the model does not account for the different internal connectivities of mobile and immobile domains. We investigate the microscale geoelectrical signature of DDMT using a pore network model (PNM) with a pipe-lattice representation of the pore space. Pore network models have been used extensively in previous petrophysical studies [e.g., *Jin and Sharma*, 1991; *Bernabé*, 1995; *Bernabé and Revil*, 1995; *Bernabé et al.*, 2011; *Suman and Knight*, 1997; *Friedman and Seaton,* 1998], and in studies of solute transport [e.g., *Dearcangelis et al*., 1986; *Bijeljic et al*., 2004; *Bijeljic and Blunt*, 2006, 2007] and multiphase flow [e.g., *Blunt et al*., 2002]. We emphasize that our present contribution is in linking flow, transport, and electrical conduction to investigate the geoelectrical signature of DDMT. Our work does not involve or require substantial advancement of pore-network simulation itself. Indeed, our approach to the electrical conduction problem is similar to those of many other studies going back decades to the work of *Greenberg and Brace* [1969]. Solution of direct-current electrical conduction and steady-state single-phase flow in a PNM are trivial. Our approach to the transport problem is somewhat novel in that we solve for temporal moments of concentration rather than for concentration itself [*Harvey and Gorelick*, 1995], reducing computational requirements and providing direct insight into DDMT behavior in the network. Although the current literature includes work involving pore-scale simulation approaches that are more advanced and rigorous than the PNM, for example, smoothed particle hydrodynamics (SPH) [e.g., *Tartakovsky et al.*, 2007] and Lattice Boltzmann (LB) [e.g., *Kang et al.*, 2002, 2006], our use of the PNM is sufficient for our purposes. For transport simulation, LB and SPH approaches offer important advantages including that they (1) do not assume Hagen-Poiseuille (laminar) flow; (2) allow for physics-based mixing at pore intersections; and (3) consider more complex pore geometries. Compared to LB and SPH approaches, however, the PNM is simple to implement and has enormous computational advantage. In our work, transport simulations are required primarily to classify pores as belonging to the mobile or immobile domain to investigate electrical averaging; that is, we require only pore residence times (or the local mass-transfer rate, the reciprocal of residence time) and do not require full, transient concentration histories throughout the network. The PNM is highly efficient for our problem and allows us to evaluate many different pore-network geometries.

5.2. Task 2A. Direct-Current Resistivity Laboratory Experiments

Controlled laboratory experiments were conducted to confirm the electrical signature of DDMT and demonstrate the use of time-lapse electrical measurements in conjunction with concentration measurements to estimate the parameters controlling DDMT, i.e., the mobile and immobile porosity and rate at which solute exchanges between mobile and immobile domains. Our experiments started with ideal materials and build up in complexity to the Hanford sediments. Initial column tracer tests (**Figure 3**) were conducted on unconsolidated quartz sand (accusand) and a material with a high secondary porosity, i.e., the zeolite clinoptilolite (**Figure 4**). During NaCl tracer tests, we collected nearly co-located bulk direct-current electrical conductivity (σ_b) and fluid conductivity (σ_f) measurements. We assumed that the NaCl solution is chemically conservative and that there is no retardation from sorption; therefore, any anomalous transport of the NaCl is attributed to physical heterogeneities, including diffusion into and out of immobile pore space.Following these initial column experiments we developed a new setup, which permitted tracer breakthrough measurements alongside CR (and hence ER) measurements on the same sample (**Figure 5**). This arrangement was used for a range of porous media, including an accusand, sieved fractions of two independently sourced clinoptilolite, glass beads, and a porous glass (in particulate form). We also revised our breakthrough analysis method by adopting an inverse approach using PEST [*Doherty*, 2010], rather than our original manual search, in order to compute best estimates of DDMT parameters [Swanson et al., in review].

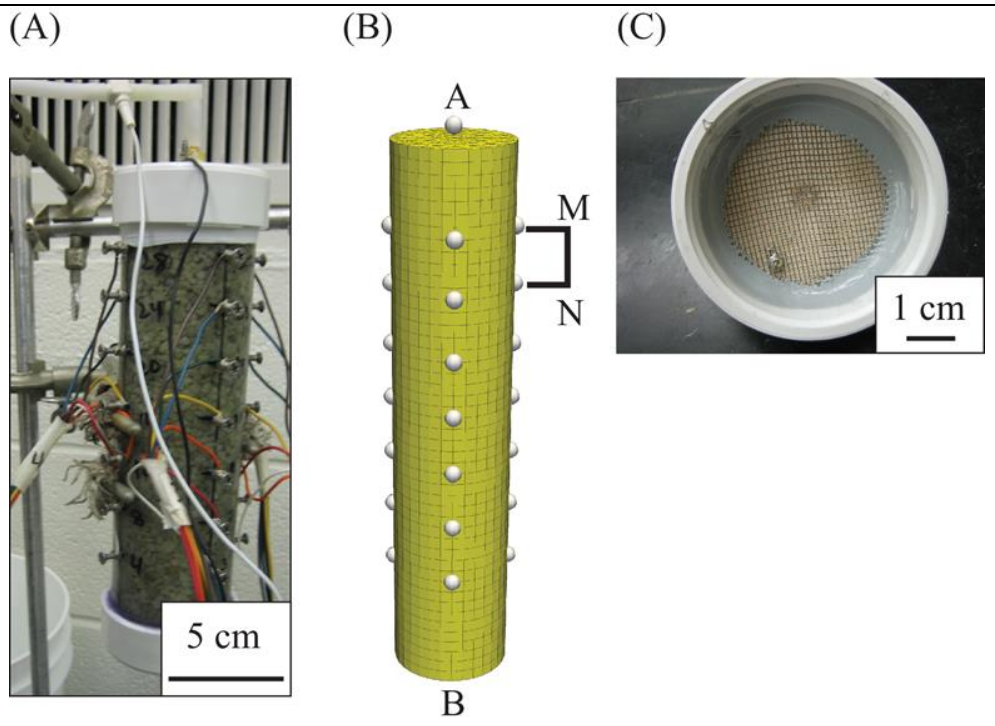

Figure 3. (A) An example column used for the tracer test showing the location of the electrodes and the fluid conductivity probe at the outlet. (B) A schematic showing potential electrodes (M,N) spaced evenly every 2.5 cm and current electrodes (A,B) at the top and

bottom of the column. The current electrode is actually a brass mesh rather than a point (C), which is placed in the end caps of the column.

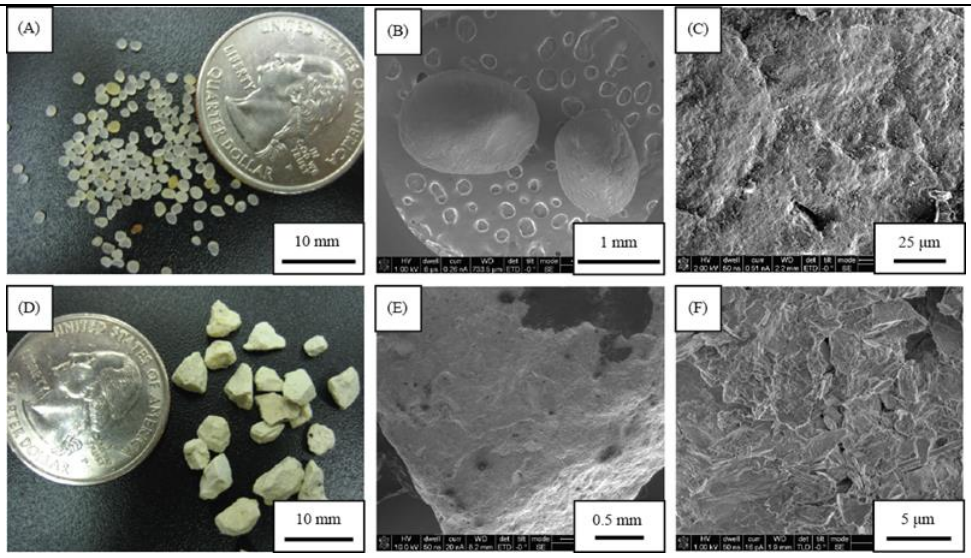

Figure 4. (A) Grains of sand consisting of over 99% silica. (B,C) SEM images of the sand grains reveal little surface topography. (D) Grains of the zeolite clinoptilolite. (E,F) SEM images of the zeolite grains show a textured surface with greater surface topography.

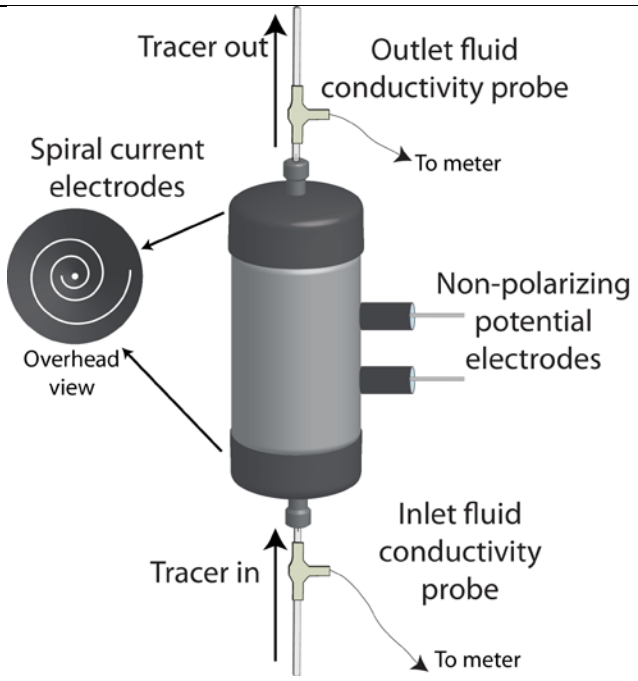

Figure 5. Schematic of column tracer setup for combined tracer and CR measurements. Fluid electrical conductivity is measured at both inlet and outlet with a micro-flow through probe (Microelectrodes, Inc.). A pair of reciprocating syringe pumps (not pictured) was used to control the flow rate.

5.3. Task 2B. Complex Resistivity Laboratory Experiments

CR measurements were collected on the same porous media as used in section 5.2 in order to explore: (1) the link between static electrical properties and physical properties influencing solute transport; and (2) the variation in CR spectra and pore fluid, in particular during a column breakthrough experiment. The column setup (**Figure 5**) permitted analysis of electrical and tracer behavior on the same sample. CR measurements were made at 23 injected frequencies in the range 2 mHz to 14 kHz. Triplicate spectra were obtained and the average spectra were modeled using the Debye decomposition approach of *Keery et al.* [2012] to determine a distribution of relaxation times, in contrast to the more commonly used Cole-Cole model [*Cole and Cole*, 1941]. Estimates of the true formation factor we determined for each column by measuring CR spectra of the saturated, packed column at seven different fluid electrical conductivities (approximately 70, 110, 155, 200, 530, 1000, and 1600 mS m^{-1}).

For analysis of tracer behavior, the solute-transport code STAMMT-L [*Haggerty*, 2009] was linked to the parameter estimation code PEST [*Doherty*, 2010] to estimate best fit single-rate DDMT parameters, θ_m, θ_{im}, and the single α, for comparison with CR results as well as NMR results (reported subsequently) and material characterization including X-ray computed

tomography (CT), SEM (e.g. **Figure 6**), mercury (Hg) porosimetry and nitrogen adsorption. This work is reported in *Swanson et al.* [in review].

5.4. Task 2C. Nuclear Magnetic Resonance Laboratory Experiments

NMR measurements were collected on the materials studied in Tasks 2A and 2B to provide independent estimates of mobile and immobile porosity. NMR relaxation data were collected with a 2 MHz Rock Core Analyzer (Magritek Ltd) using a CPMG (Carr-Purcell-Meiboom-Gill) pulse sequence. For each sample, 40 data points were obtained at each echo, and 50000 echoes were collected with an echo spacing of 300 μs. Each set of measurements was stacked 32 times with a delay time of 10 s. The T_2-distribution was determined by applying a non-negative least squares inversion with Tikhonov regularization to a logarithmically subsampled set of the NMR data [*Whittall et al.*, 1991]. The regularization parameter was selected such that each datum was misfit by approximately one standard deviation.

The distribution of relaxation times can be used to approximate the total θ_m and θ_{im} and provides an independent estimate that can be compared to the values determined using the curve-fitting methods. The total porosity can also be estimated from the NMR data for each sample by measuring the initial signal amplitude, converting to the total water volume using an instrument-specific calibration factor, and then converting the total water volume estimate to total porosity by adjusting for the known total volume of the sample holder. NMR measurements were repeated three times, and the total, less-mobile and mobile porosities were calculated separately for each sample. Aspects of this work are found in Swanson et al. [2012] and Swanson et al. [in review].

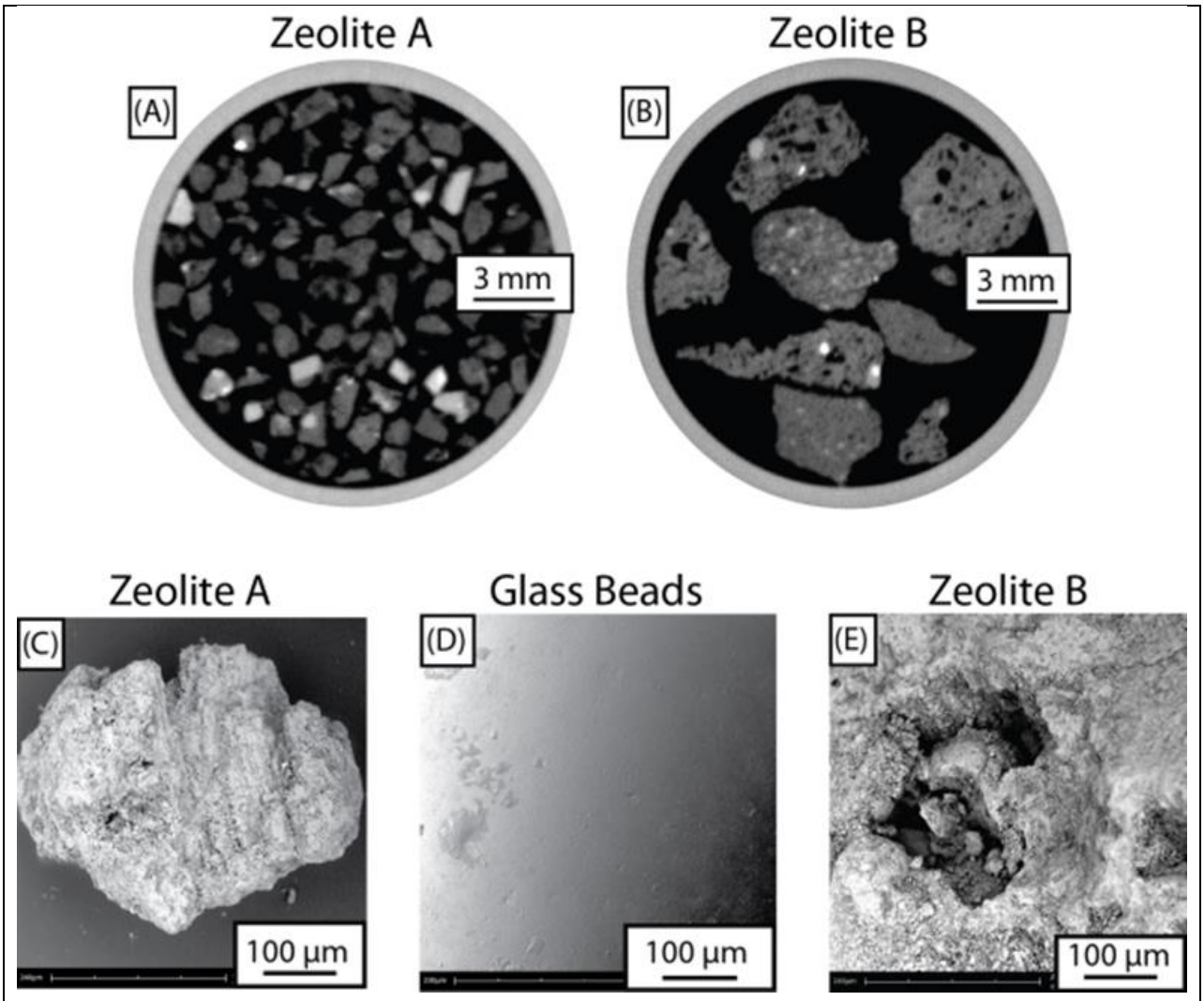

Figure 6. Example CT and SEM images of some of the materials used. The synthetic, non-porous, glass beads were used as a control, and two zeolites were sieved to 5 different sizes. CT (A, B) and SEM (C-E) images show the different intragranular pore structures between the two zeolites and the lack of intragranular pore structures in the glass beads. CT scans were conducted in a graduated cylinder and not in the column used for tracer experiments, and include all of the sieved fractions.

5.5. Task 3A. Field-scale Experiments at the Hanford 300 Area, Hanford, WA

Originally, our field plans focused on electrical monitoring of tracer tests at the IFRC well field. However, in light of PNNL's borehole-flow mitigation plans, which involved grouting wells, we shifted our focus to the shallow subsurface at the IFRC. Formulated after discussions with PNNL scientists and DOE managers, our field experiments included vertical infiltration and tracer experiments monitored using electrical and thermal methods, as well as conventional fluid

sampling. In March 2012, we installed probes at the Hanford IFRC well field for time-lapse electrical and chemical monitoring of vertical infiltration and tracer experiments. Probes include 10 stainless-steel electrodes at 1-foot spacing, three fluid-sampling ports, and four thermistors. Double-ring infiltration experiments were first using freshwater to saturate below the infiltrometer, and later an ionic (NaBr) tracer in July 2012 (**Figures 7, 8**).

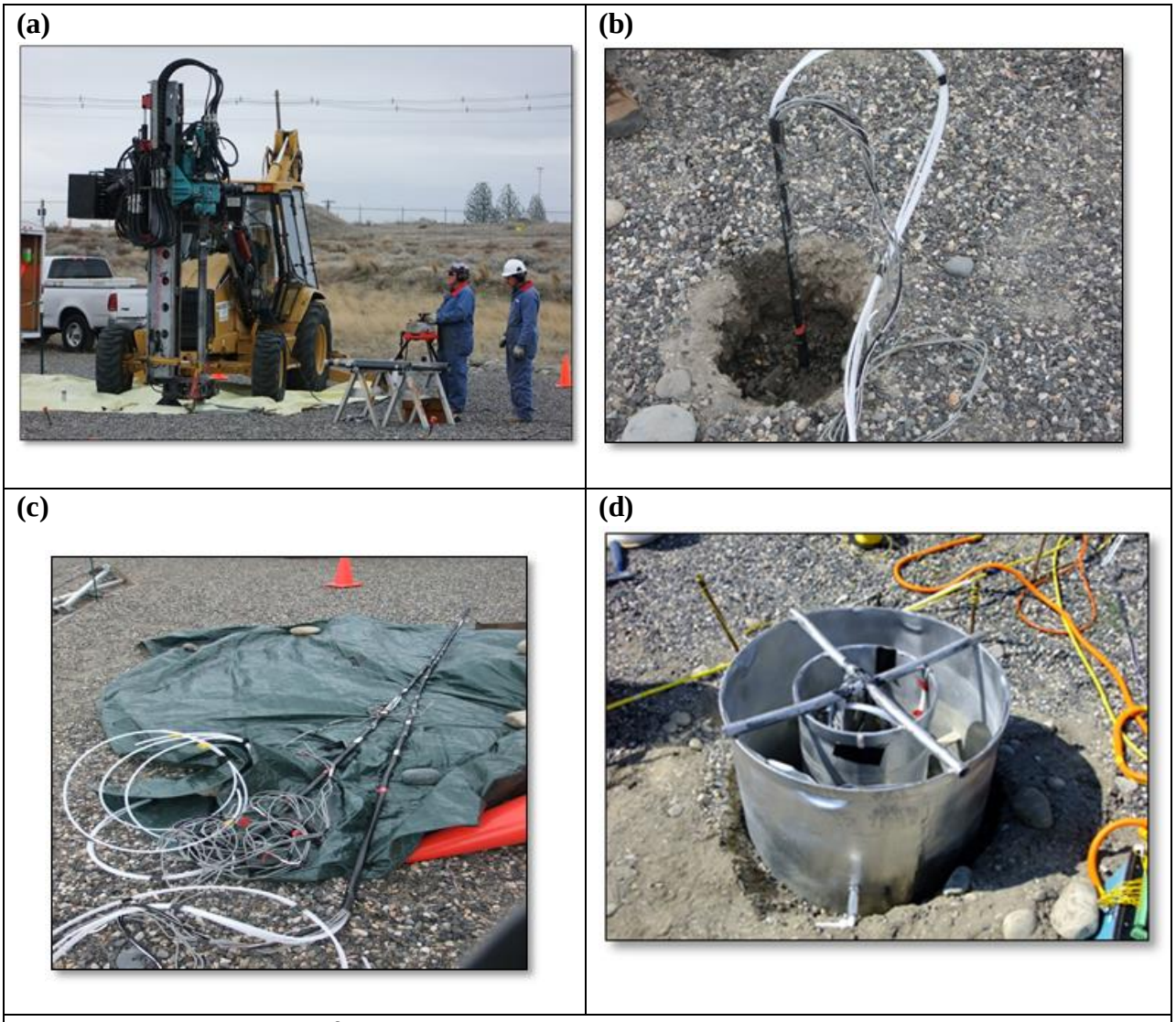

Figure 7. (a) Installation of electrodes and sampling ports by direct-push technology; (b) electrode cables and sampling ports at the probe head up-hole; (c) photograph of field setup before deployment, comprising electrodes and sampling ports on a collapsible fiber-glass backbone; and (d) double-ring infiltrometer.

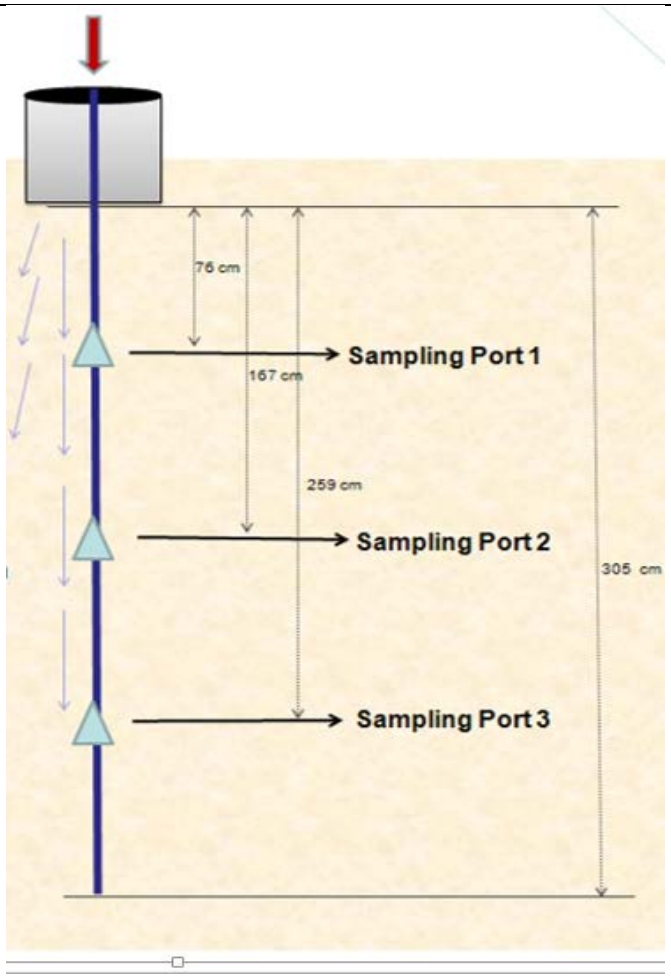

Figure 8. Schematic diagram of experimental setup. Electrodes are located at 30-cm intervals from 10 to 300 cm depth below ground surface.

5.6. Task 3B. Field-scale Experiments at the Naturita UMTRA Site, Naturita, CO

Under a separate DOE SBR grant (DE-SC0003681) awarded to G. Curtis (USGS) with co-PIs from this grant (Day-Lewis and Lane), tracer-test monitoring was conducted at a former uranium mill tailings site in Naturita, Colorado. The overall goal of this work was to investigate heterogeneity, but we designed piggybacked experiments to enable analysis for mass transfer after complicated with access at Hanford. We conducted a forced-gradient tracer experiment at a radionuclide-contaminated site and monitored tracer transport by conventional fluid sampling and concurrent geoelectrical measurements.

Ten polyvinyl chloride (PVC) fluid/geoelectrical monitoring wells and an injection gallery were installed using a Geoprobe direct-push rig. Each monitoring well consists of fifteen 2.5 cm wide, 4.1 cm diameter, stainless steel electrodes spaced 22 cm apart, and four levels of 0.64 cm diameter sampling ports spaced 30.5 cm apart, installed to a total depth of

approximately 5.5 m below ground surface. Wells were installed a meter apart in the east-west direction and spaced two meters apart in the north-south direction (**Figure 2**). The injection gallery consists of nine 0.75-in diameter wells, installed to depths of approximately 4.5 m with 0.6 m screen the bottom of each well. The injection wells are distributed in two rows, spaced 0.5 m apart.

Figure 9 shows the conceptual injection experiment as a 2-D cross section, and how the experiment is reduced to a 1-D transport problem between the injection gallery and co-located fluid conductivity (σ_f) and bulk conductivity (σ_b) observation locations distributed along vertical arrays. Forced injection, at a rate of 0.9 ± 0.1 L/min, was conducted for 27 days from October 27th to November 19th, 2011. A NaCl tracer solution (8420 ± 330µScm^{-1}) was injected for 15 days, and followed directly by a freshwater flush injection (360 ± 5 µScm^{-1}) for 12 days. Groundwater fluid parameters (specific electrical conductivity, pH, and temperature) were measured once per day using an Orion 5-star meter, conductivity change resulting from the tracer addition was assumed to be conservative. The meter was calibrated daily for electrical conductivity and pH. Prior to sampling, sampling ports and tubing were purged using a peristaltic pump. All fluid conductivity measurements, σ_f, were converted to a reference temperature equal to the mean groundwater sample temperature (14.5 $^{\circ}$C), to make fluid measurements comparable to the geoelectrically measured bulk conductivity measurements, σ_b.

Single-borehole 4-electrode resistivity profiles were collected twice daily for every monitoring well vertical profile. Wenner-style measurements [e.g. *Telford et al.*, 1990] were collected using a SuperSting R8 IP (Advances Geosciences, Inc.) 8-channel resistivity meter. For comparison of fluid-sampling and geoelectrical measurements, a petrophysical model is required. In this work, we assumed the bicontinuum model of Singha et al. [2007], in which mobile and immobile domains act as conductors in parallel.

Groundwater flow and solute transport were simulated in using the finite-difference model MODFLOW-2000 [*Harbaugh et al.*, 2000] combined with particle tracking in MT3DMS [*Zheng and Wang*, 1999] to solve the one-dimensional (1-D) advective-dispersive transport equation with DDMT. The mass-transfer parameters (and diffusion coefficient) were optimized through nonlinear regression with UCODE_2005 [*Poeter et al.*, 2005; *Hill and Tiedeman*, 2007] using MATLAB (Mathworks, Inc., Natick, MA) codes in an intermediate step to generate the necessary input text files from forward model output. The σ_f and σ_b observations from each location were typically given a coefficient of variation (CV) weighting of 3%, or the general estimated error in conductivity observations based on inspection of repeat and reciprocal errors.Non-linear regression was used to calibrate dual-domain mass-transfer solute-transport models jointly to solute and electrical field data. This method differs from previous approaches by calibrating the model simultaneously to observed fluid conductivity and geoelectrical tracer signals using two parameter scales: effective parameters for the flowpath upgradient of the monitoring point, and the parameters local to the monitoring point (**Figure 9**). Regression statistics allowed for rigorous evaluation of the information content and sensitivity of the geophysical data. This work was reported in Briggs et al. [2012], and additional work will be found in Briggs et al. [in prep].

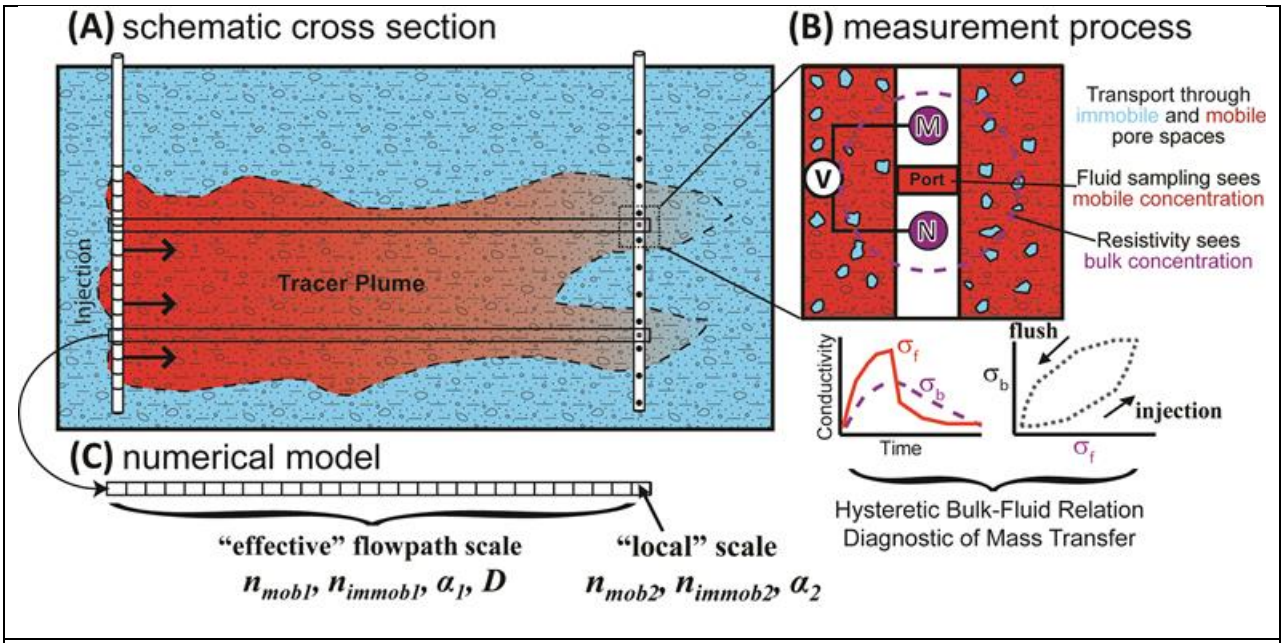

Figure 9. Schematic diagram of (A) the field-scale tracer injection which was observed in full at a subset of the original monitoring points; (B) the local-scale co-located fluid (σ_f) and bulk (σ_b) conductivity sampling and associated hysteresis resulting from mass transfer; and (C) the 1-D numerical model framework partitioned into effective upgradient-flowpath and local-scale parameter sets.

6. Results

Results of our work are presented according to the three majors tasks in our work plan.

6.1. Task 1. Numerical and Analytical Modeling & Tool Development

Methods development under this grant included development of codes for data analysis used in Swanson et al. [2012; in review], Briggs et al. [2013; in prep], and Keery et al. [2012]. Methods included integration of model-calibration tools (PEST, UCODE_2005) with solute-transport codes and decomposition of CR spectra. These developments are detailed elsewhere in this report, where applied to laboratory or field data.

In a publication currently in preparation and an important product of this work, we developed a pore network model (PNM) approach, which includes seven steps, illustrated schematically in **Figure 10**. In Step 1, we generate a pore network, drawing the geometric characteristics of the pores and connecting pore throats from random distributions. In Step 2, we solve the flow problem for head; calculate the upscaled, effective hydraulic conductivity; and calculate inter-pore flows for use in transport simulation. In Step 3, we solve a transport model for temporal moments of concentration and calculate maps of mass-transfer rates. In Step 4, we assign pores to mobile or immobile domains using an algorithm that ensures percolation and internal connectivity of the mobile domain. The upscaled, effective mass-transfer rate for the

medium is calculated from the distribution of rates in the network. In Step 5, we simulate a column tracer experiment to produce mobile- and immobile-domain fluid-conductivity breakthrough curves; these time-varying conductivities are used as input to the electrical-conduction pore-network model. We solve for the effective electrical conductivity of the network over time to produce the bulk/fluid conductivity relation. Last, in Step 7, we compare alternative petrophysical models to the simulated bulk/fluid conductivity relation and assess the relative merits of the models considered. The 7-step procedure is repeated for different pore-network geometries.

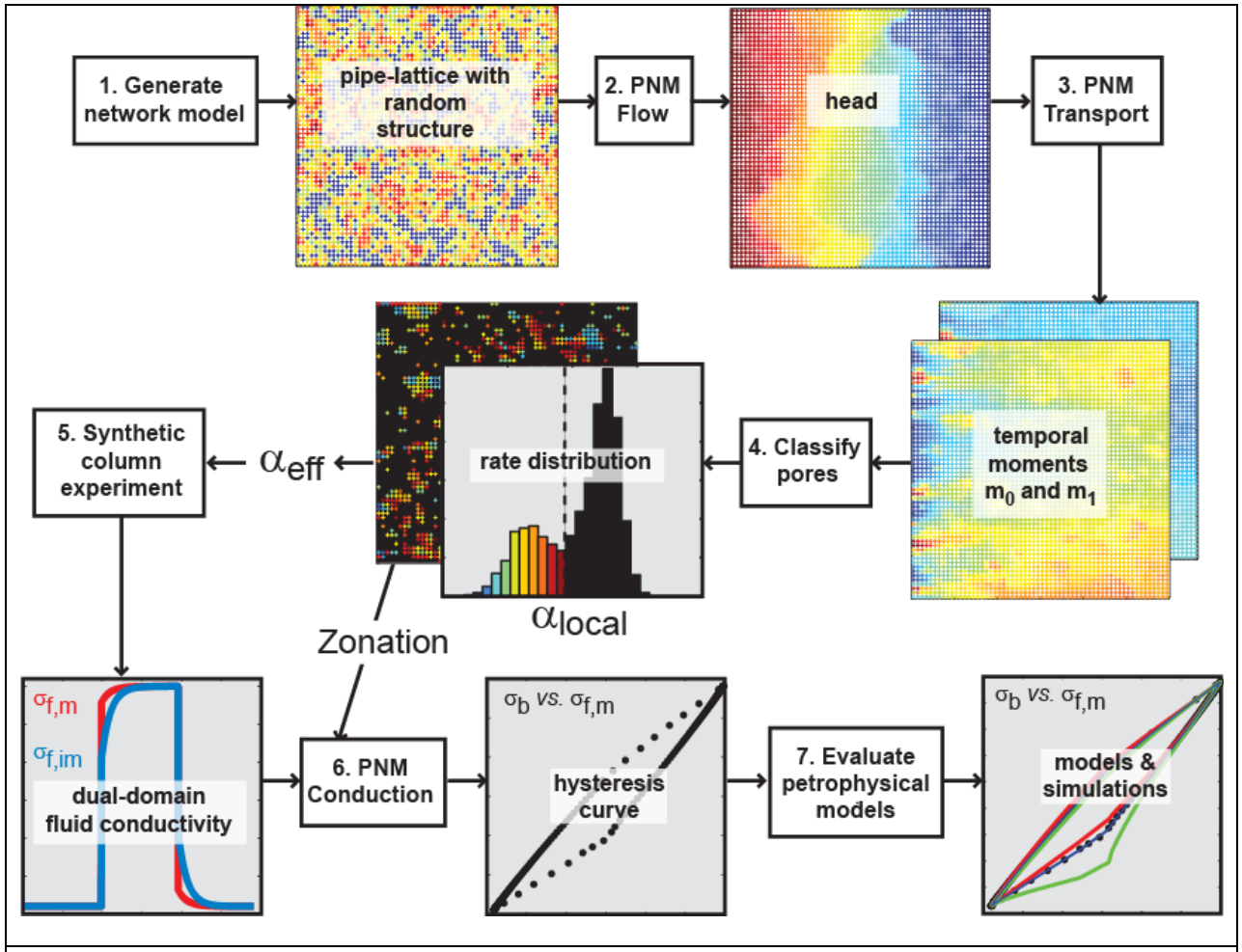

Figure 10. Schematic diagram illustrating our 7-step approach to evaluate the geoelectrical signature of dual-domain mass transfer for different pore-network models.

The pore network consists of a lattice of pipes with rectangular cross sections of variable area. A two-dimensional (2D) lattice is considered here, although the calculations are performed in three dimensions (3D) assuming equal pore widths in the *x* and *y* directions; hence the model operates in 3D but we consider only single-layer networks in this work. Cross-shaped pore bodies are connected by smaller pore throats (**Figure 11**). For simplicity, we assume uniform

length, and so a regular grid. In Step 1 of our approach (**Figure 10**), we generate models by drawing pore and throat sizes from random distributions. A range of models are considered with different geometric characteristics (e.g., distributions of pore size, throat size, etc.), enabling us to investigate a range of averaging behaviors. We assume a coordination number of 4 (i.e., every pore is connected to the four adjacent pores in the 2D lattice), but pores connected by small pore throats effectively are isolated from one another.

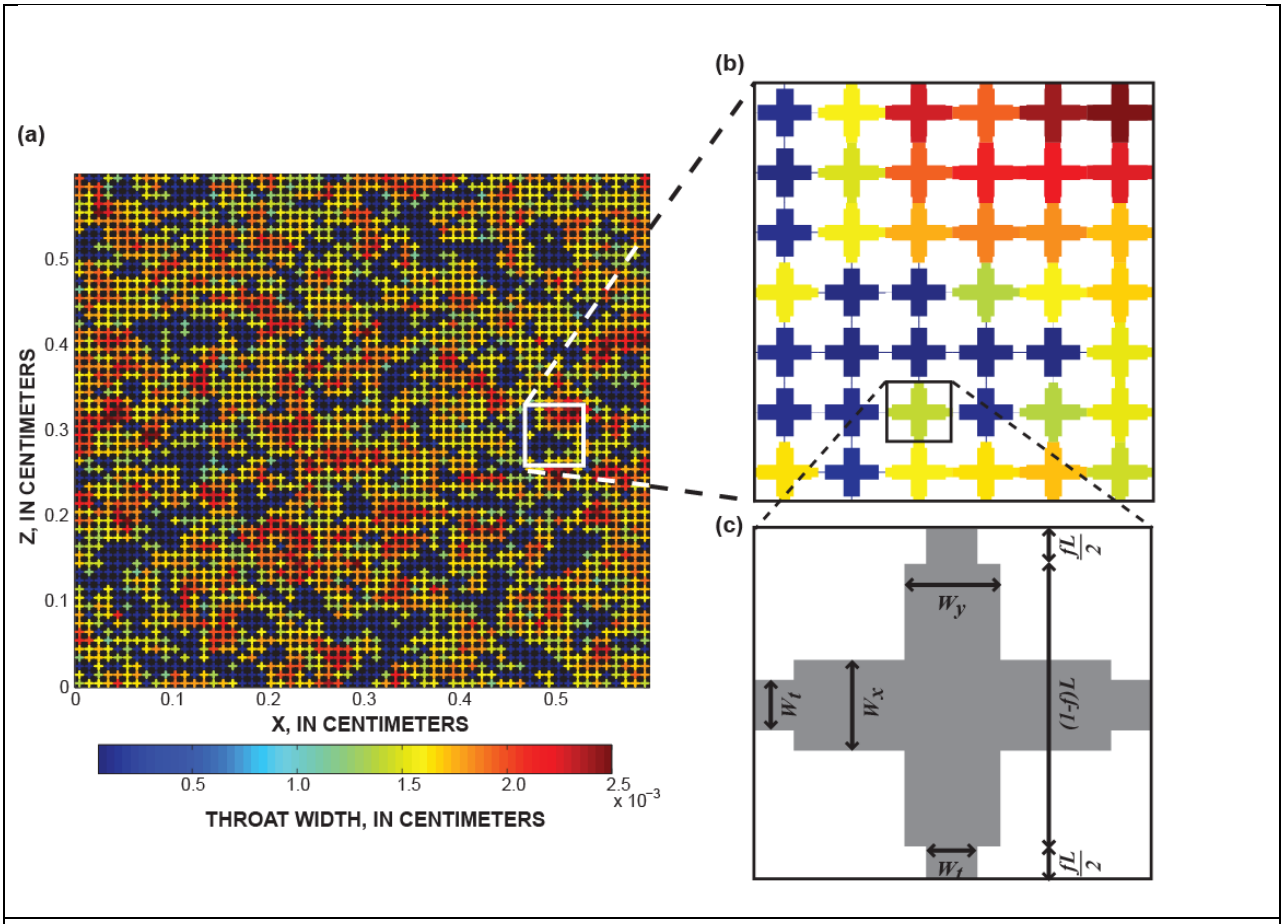

Figure 11. Schematic diagram showing the pore-network model architecture, which consists of a network of pipes. Each pore is represented by a cross-shaped intersection of two pipes of widths W_x and W_y in x and y directions, respectively, with adjacent pores connected by smaller throats of width W_t. Pore bodies occupy a fraction, f, of the total length, l, of the pore, with the pore throats occupying the remaining $(1\text{-}f)l$ in each direction. Pipes with rectangular cross sections are assumed.

PNM simulations have been performed for a range of network geometries. Work is ongoing to test alternative petrophysical models against PNM results, to understand the range of applicability of the bicontinuum and other models. Results for one geometry are shown in **Figure 12**.

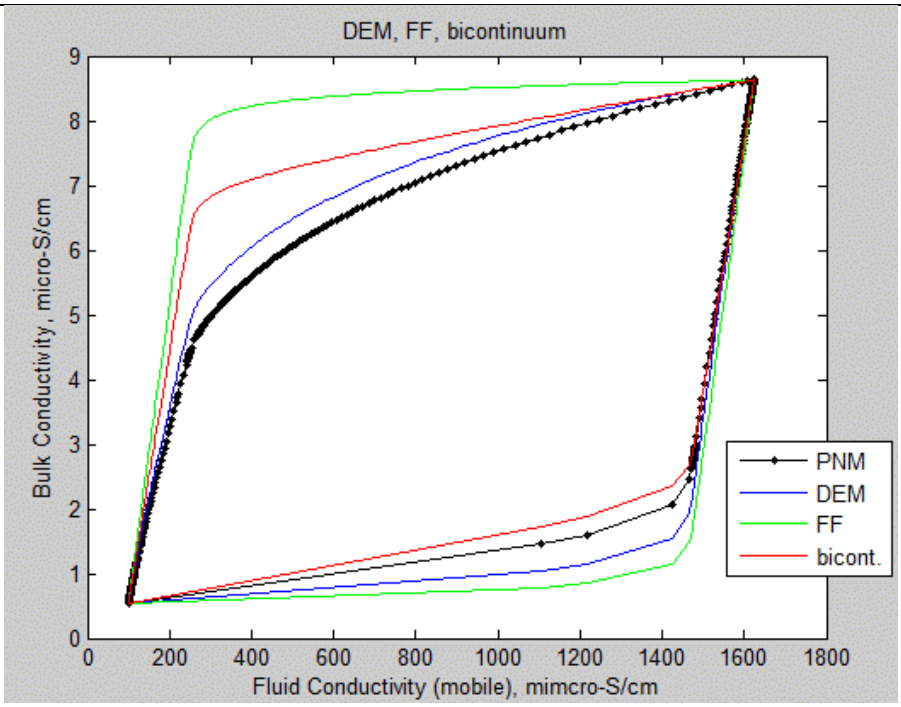

Figure 12. Example pore-network model simulations (PNM) of bulk vs. fluid conductivity and model fits for differential effective media theory (DEM), the free-phase model (FF), and the bicontinuum model of Singha et al. (2007).

6.2. Task 2A. Direct-Current Resistivity Laboratory Experiments.

We presented the first controlled, laboratory experimental evidence confirming that the synthesis of σ_f with σ_b can be used to directly estimate parameters controlling the operation of mass transfer in Swanson et al. [2012]. Our results for the zeolite show (1) extensive tailing (**Figure 13)** and (2) a hysteretic relation between σ_f and σ_b, thus providing evidence of mass transfer not observed within the quartz sand, which had negligible tailing. The hysteresis between σ_f and σ_b observed in the zeolite tracer test is evidence for the exchange of solutes between and immobile and mobile domain, and cannot be explained by large-scale heterogeneity, or by the difference in measurement scales of σ_f and σ_b. In the sand column, we did not observe any hysteresis between σ_f and σ_b, consistent with advection-dispersion behavior with negligible mass transfer.

To identify best-fit parameters and evaluate parameter sensitivity, we performed over 2700 simulations of σ_f, varying the immobile and mobile domain and mass transfer rate. We emphasized the fit to late-time tailing by minimizing the Box-Cox power transformed root-mean-square error between the observed and simulated σ_f to emphasize the late-time tailing behavior. The mass transfer rate is the parameter that has the most influence on the anomalous, late-time

tailing behavior. For the zeolites, we present a best-fit mobile and immobile porosity of 46% and 20%, respectively, and a mass transfer rate of 10^{-5} s^{-1}. This is similar to our NMR estimates for a mobile and immobile porosity of 43% and 7.7%, respectively. For the sand, we present a best-fit mobile and immobile porosity of 33% and 1%, respectively, and a mass transfer rate of 10^{-5} s^{-1}. This is consistent with our NMR estimates for a mobile and immobile porosity of 31% and 0.7%, respectively. These sorts of measurements can be made from field sites such as Hanford or Naturita. This work was reported in Swanson et al. [2012].

The zeolites were also sieved to identify possible correlation between grain size and DDMT parameters because analysis of multiple sieved fractions allows for more robust assessment of correlation than would be possible given only the two samples of two different grain sizes. DDMT model estimates of θ_m and θ_{im} for Zeolite A (fine) were similar across all three sieved fractions (**Table 1**). Similarly, model estimates of θ_m and θ_{im} for Zeolite B (coarse) were similar, however, smaller θ_m and greater θ_{im} were observed for this zeolite compared to Zeolite A (total porosity for the two zeolites were similar). The substantial differences in each of the DDMT parameters between zeolite A and B are attributed to the different intragranular pore structure of the two zeolites given their different origins, rather than grain size (e.g. **Figure 6**).

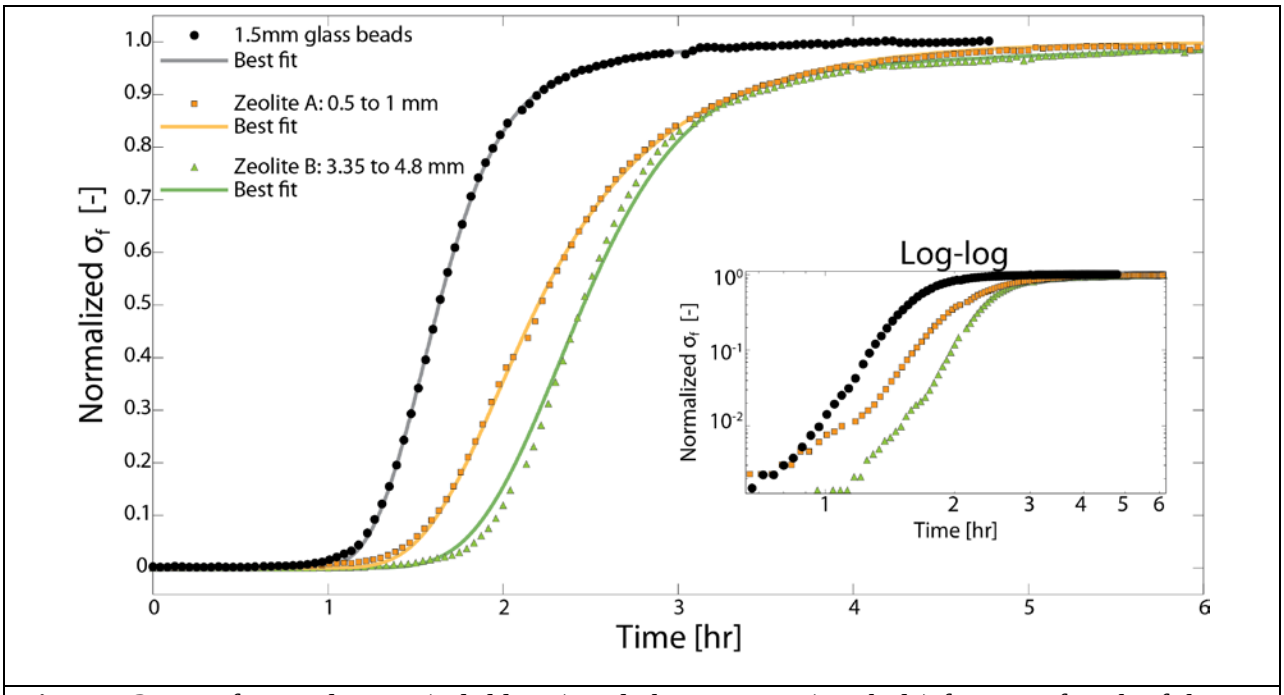

Figure 13. Best fit simulations (solid lines) and observations (symbols) for one of each of the zeolite sub-fractions and the glass beads, with a subset showing the log-log response. The three different materials used have different breakthrough curve (BTC) responses, indicating different mass transfer properties. Earlier arrival is indicative of a smaller θ_m. The effect of mass transfer appears in the two zeolites as tailing and the gradual increase in normalized σ_f until the input σ_f is reached. The subset image shows the response log-log space without the best fit forward simulations.

Table 1 shows a summary of DDMT breakthrough analysis for selected column experiments alongside electrical properties determined from measurements of bulk electrical conductivity with varying fluid electrical conductivity. In **Table 1**, σ_s is the surface electrical conductivity, F is the true formation factor and G is the electrical connectedness [as defined by *Glover*, 2010]. We see that this latter value appears to give an indication of the mobile porosity, which in the case of Zeolite A clearly includes a significant intragranular component. We believe that this electrical property helps differentiate the contrasting intragranular structures of the two zeolites, in particular that although both have similar total porosity and the grains of Zeolite B have larger internal pores (see, for example, **Figure 5**), a significant element of the intragranular porosity in Zeolite B does not contribute to solute transport.

Table 1. Transport model and ER results for selected zeolite and glass bead column experiments.

		Zeolite A			Zeolite B		Glass beads
	Sieved fraction [mm]	**0.25 to 0.5**	**0.5 to 1**	**1 to 2**	**2 to 3.35**	**3.35 to 4.8**	**1.5**
Transport	Log_{10} α [s^{-1}]	-3.7	-3.9	-4.1	-3.5	-3.3	-3.3
	θ_m [-]	0.57	0.58	0.61	0.45	0.48	0.39
	θ_{im} [-]	0.04	0.04	0.04	0.09	0.08	0.01
	$\theta_m + \theta_{im}$ [-]	0.61	0.62	0.65	0.54	0.56	0.40
	Gravimetric θ [-]	0.69	0.68	0.68	0.64	0.64	0.42
DC Resistivity	σ_s [mS m^{-1}]	11	12	10	12	10	0.2
	F [-]	2.8	2.9	2.7	3.7	3.4	3.9
	G [-]	0.36	0.34	0.37	0.27	0.29	0.26

6.3. Task 2B Complex Resistivity Laboratory Experiments

Measurements of static properties

We obtained samples of 6 sieved fractions (clay to very coarse sand) from the Hanford IFRC wells. These were used for initial exploration of the link between physical properties of the sediments and CR spectra. Measurements revealed (as expected) a progressive increase in total polarization and a shift towards higher frequency peak response with progressively finer

grain size (**Figure 14**), reflecting the increase in surface area and associated shorter relaxation time with finer grains.

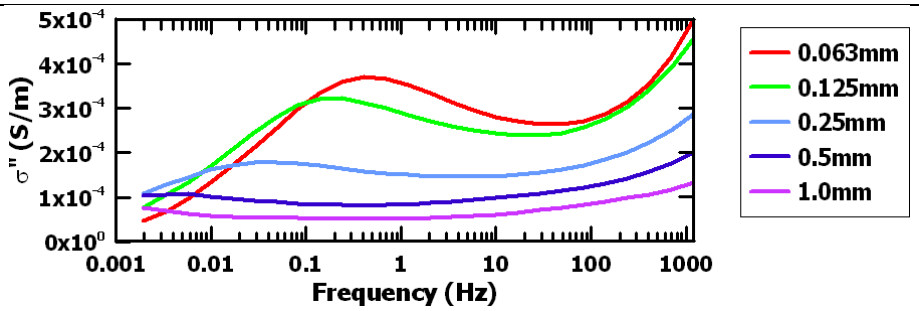

Figure 14. Imaginary conductivity spectra for five sieved fractions saturated with 0.01M NaCl. Spectra for the finest (clay) fraction, which reveals much higher imaginary conductivity, has been omitted in order to see clearly the variability of the other samples within one plot.

Assuming a grain surface polarization model, the contribution of each particle to polarization should be weighted according to its surface area. If we adjust the particle size distribution according to particle surface area we see a significant contribution to total surface area from the very fine particles. We recognize that this may be somewhat exaggerated from the particle size analysis as these particles probably act as an enhanced surface roughness under normal conditions (such as during the measurement of CR spectra) but are dislodged under the particle size analysis process. Using Keery's Debye decomposition model, and assume a surface diffusion coefficient, D, for Na^+ (we assume D = 1.33 x10^{-9} m^2s^{-1}), we can convert each relaxation time interval into an effective length. This then provides a distribution of relaxation length scales, based on total polarization (chargeability). **Figure 15** below shows an example of such a distribution, and compares this to the particle size distribution weighted according to total surface area. The bimodal distribution is remarkably similar, with reasonable consistent modal values, again supporting the goal of predicting the textural contribution to the CR spectra in such a porous media. From this we can postulate that if solute transport is controlled by the grain texture of the porous media, CR spectra may have value in providing undisturbed measure of relevant textural properties. However, as we see later, in the presence of significant intragranular porosity which contributes to mass transfer, this may have limited value.

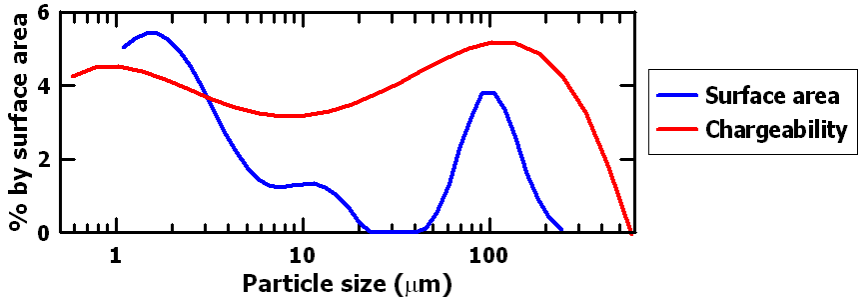

Figure 15. Comparison of measured particle size (expressed as percent by surface area) and polarization contributions (from Debye decomposition of CR spectra) for the sieve 230 (63 μm – 125 μm) fraction.

Measurements of CR spectra on Hanford IFRC sieved samples saturated with different fluids revealed that the saturating fluid has a clear, and measurable, impact on the CR spectra and the effect appears to be influenced by the texture of the porous medium (see **Figure 16**). Whilst KCl and $CaCl_2$ both show a reduction in polarization, reflecting different mobilities, there is a clear shift in the distribution of relaxation times for the finer grained sample (compare (A) and (B) in **Figure 16**). The results suggest that cation exchange processes under solute transport are measurable with CR spectra, however, we need to explore physically-based mechanisms that can describe the observed behavior.

(A)

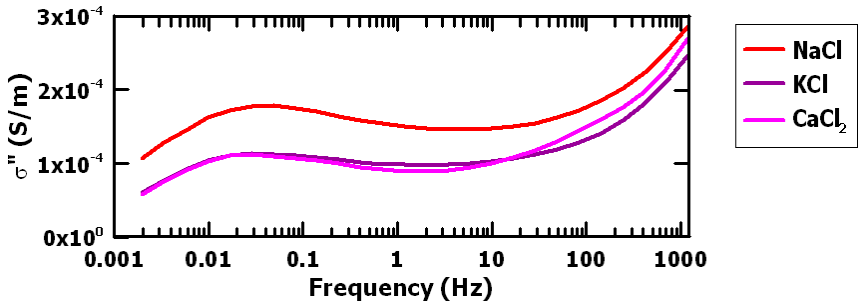

(B)

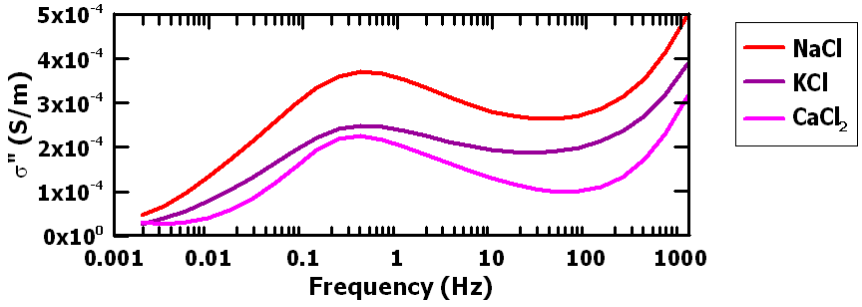

Figure 16. Effect of saturating fluid on CR spectra for (A) sieve 60 (250 μm – 500 μm) fraction and (B) sieve 230 (63 μm – 125 μm) fraction. All saturating fluids are 0.01M.

Links to tracer behavior

Our analysis of solute transport at the laboratory scale, which is reported in *Swanson et al.* [in review] has focused on the zeolite clinoptilolite, since it contains a significant

intragranular porosity. Sieved fractions of two independently sourced clinoptilolites were compared against a glass bead porous media reference. Based on CT and SEM images, coupled with Hg porosimetry and N adsorption data, **Figure 17** shows how the physical structures of the porous media contrast.

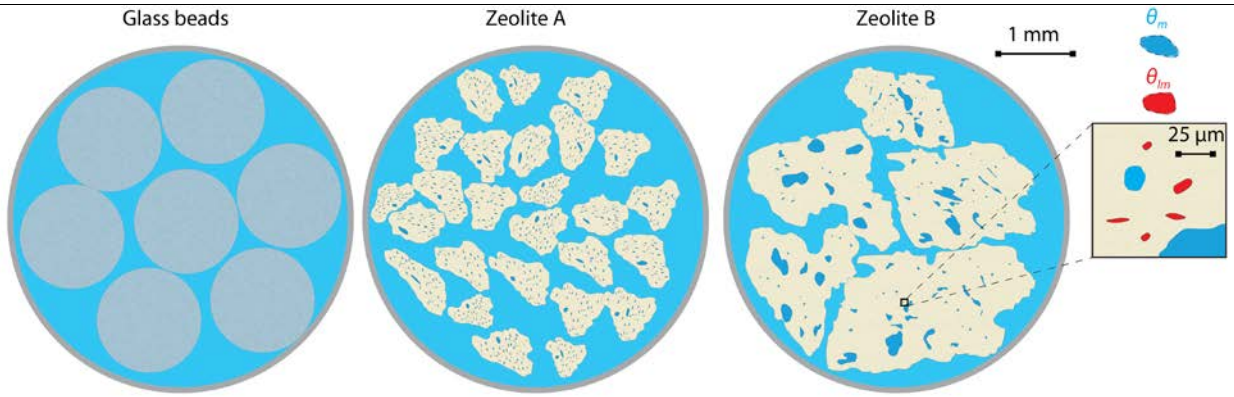

Figure 17. A schematic representation of the three different materials considered, based on CT images, geophysical and transport data, and our understanding of the pore structures. The smallest pores, which are assumed to not be active for transport, are not visible at this scale. The glass beads have little immobile porosity and mass transfer. Zeolite B has large intragranular pores throughout the entire grain that have a low degree of connectivity. Zeolite A has a greater connectivity and a slightly smaller immobile porosity. The connectivity of the pores extends normal to the page for the zeolites. The subset shows the enlarged schematic image of the coarse zeolite with the less-mobile pores with the size representative of the transport and Hg porosimetry results.

In contrast to CR measurements on the glass bead samples, the CR spectra for the zeolites revealed significant polarization, which is consistent with the observed surface electrical conductivity (**Table 1**) and large surface area (measured by nitrogen adsorption). However, as shown earlier for the Hanford IFRC sieved samples, the spectra of Debye relaxation times appears to be dominated by an effective grain size. For both zeolites, finer sieved fractions revealed a shorter peak relaxation time (**Figure 18**). However, it is clear from the solute tracer analysis that a significant proportion of intragranular porosity contributes to tracer movement (which is backed up by the electrical connectedness, *G*) and thus this dominant relaxation time in the CR spectra may be of limited value for understanding DDMT. However, we note that the zeolite with greater electrical connectedness and larger intragranular pore space active in solute transport (Zeolite A) also exhibits a greater contribution to total polarization at time scales much shorter than that representative of the grain scale. We, therefore, propose that the CR do provide additional evidence of electrical connectedness at the sub-grain scale, which, in turn, may influence DDMT behavior.

It is also worth noting that CR measurements (specifically the imaginary conductivity) may be valuable in improving estimates of the true formation factor (and hence connectedness, *G*) in-situ, since the real conductivity at low pore water conductivity can be strongly influenced by surface conductivity, the effect of which needs to be removed.

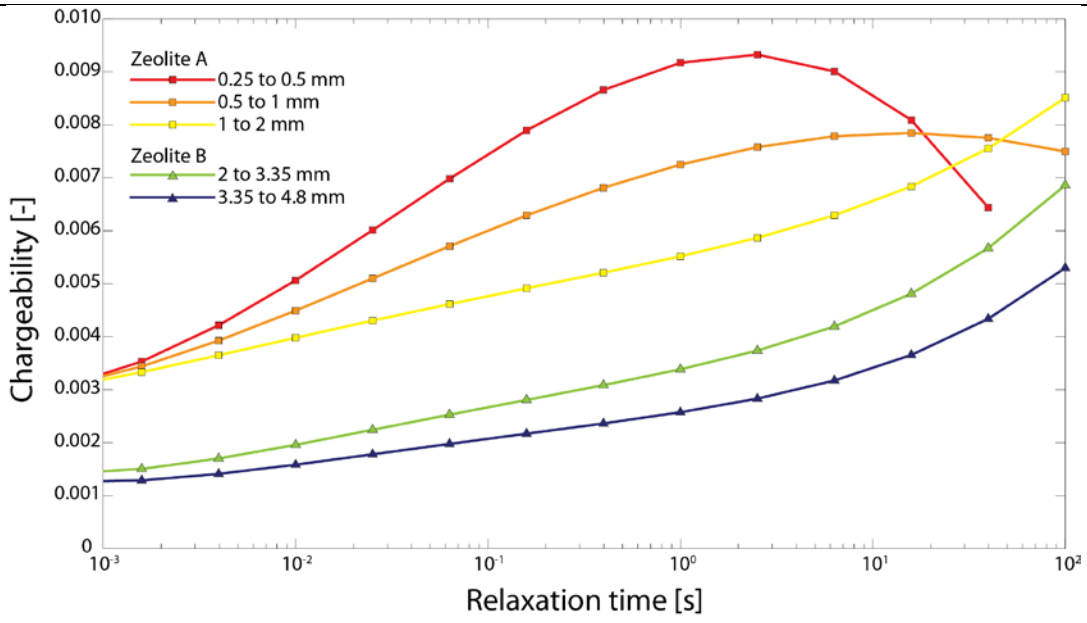

Figure 18. Spectra of Debye relaxation times from CR spectra for the two zeolites. The response at larger relaxation times corresponds to a grain size effect, whereas the response at smaller relaxation times appears to correspond to a difference in the pore structures. There is a distinct difference between the two zeolites for the smaller relaxation times.

6.4. Task 2C. Nuclear Magnetic Resonance Laboratory Experiments

NMR measurements were made on samples from the column tracer experiments and packed to the same equivalent porosity. The NMR relaxation time distributions (**Figure 19**) are strongly dependent on material type. The NMR relaxation time distribution for the glass beads is, as expected, dominated by a large peak at long relaxation time that is assumed to correspond to intergranular pore water. Conversely, for Zeolite A and Zeolite B, relaxation occurs with both long and short relaxation times, suggesting intragranular pore space. The shape of the distributions implies that Zeolite A has a more continuous pore size distribution compared to Zeolite B.

We found that translating the 3 and 33 ms cutoff times to divide the total porosity into either θ_{im} or θ_m is weakly supported [*Swanson et al.*, 2012]. The total porosity determined by the sum of transport-model calibrated θ_{im} and θ_m from tracer tests may not be the same as the gravimetric porosity because of a totally disconnected pore space θ_{dc} , which does not contribute to transport. NMR may be sensitive to these pores; therefore, a single cutoff time dividing the

NMR relaxation time distribution into either θ_{im} and θ_m may be insufficient for modeling transport. Another cutoff time may be needed to account for θ_{dc}. We define the total gravimetric porosity, θ_{tot} [-], as the sum of θ_{im}, θ_m, and θ_{dc}.

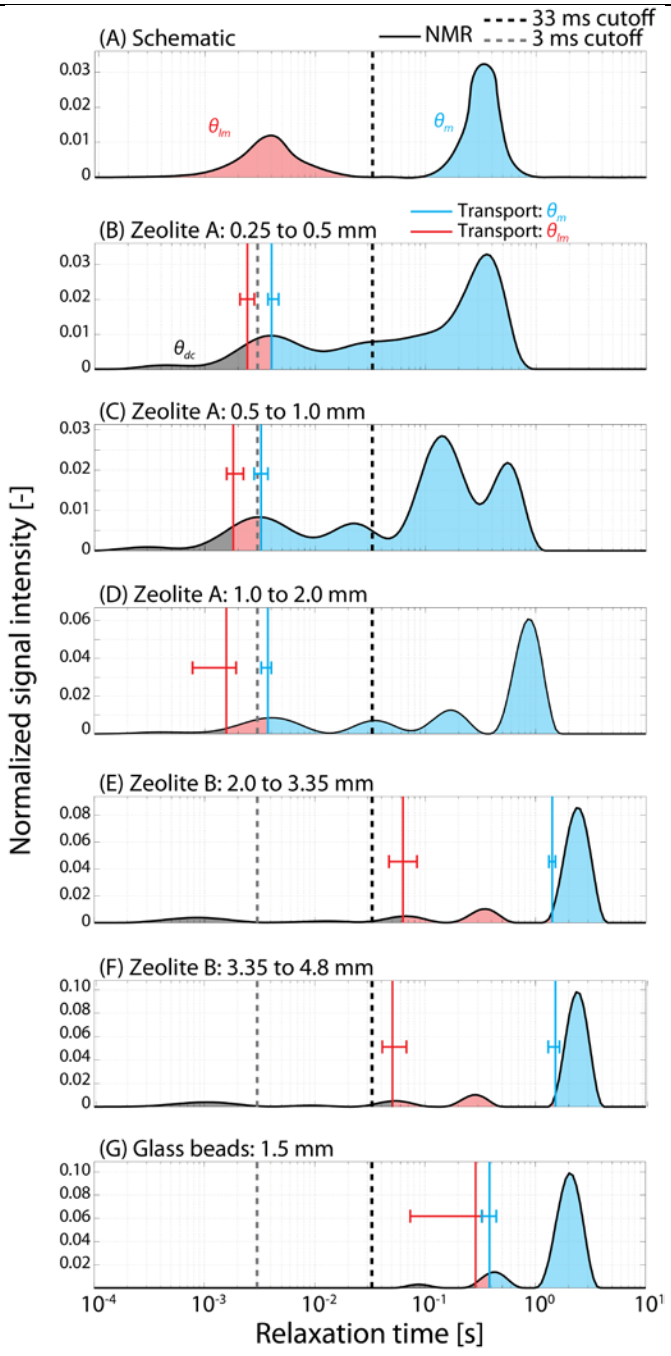

Figure 19. (A) The schematic shows an idealized NMR relaxation time distribution dominated by two distinct peaks that would correspond to θ_m or θ_{im}, given by a single cutoff time. In the subsequent subplots (B-G), the NMR relaxation time is shown for each of the samples. The 3 and 33 ms cutoffs do not fall in natural breaks of the NMR relaxation time distributions. The

transport-estimated best fit θ_m and θ_{im} are shown as blue and red lines, respectively, with associated error bars assuming a 1% error in the transport-model calibrated θ_m and θ_{im} [from Swanson et al.,in review].

Appropriate cutoff values are likely dependent on the connectedness of the pore structures, which are material dependent. The ideal NMR cutoff times that match the transport-model calibrated θ_m and θ_{im} (**Figure 19**) are determined by first fitting the θ_m assuming large pores are mobile, then fitting θ_{im} assuming shorter times are less-mobile and finally assuming the rest of the signal corresponds to disconnected pore space. These estimated cutoff times are close to the 3 ms cutoff in Zeolite A, but are near 1.5 s in Zeolite B. The NMR relaxation time distribution is more multimodal in Zeolite A than B, which we believe is consistent with our developed conceptualization of the two porous media: both have a large intragranular porosity but Zeolite B has less sub-grain pore connectivity.

6.5 Results of Tasks 2A-C.

Figure 20 summarizes our conceptualization of these contrasting zeolites. Used in isolation the geophysical measurements may have limited value in characterization of pore structure relevant to solute transport, but, as our results show [and in more detail in *Swanson et al.*, in review] the combined used of NMR and electrical measurements can offer considerable insight into relevant material characteristics.

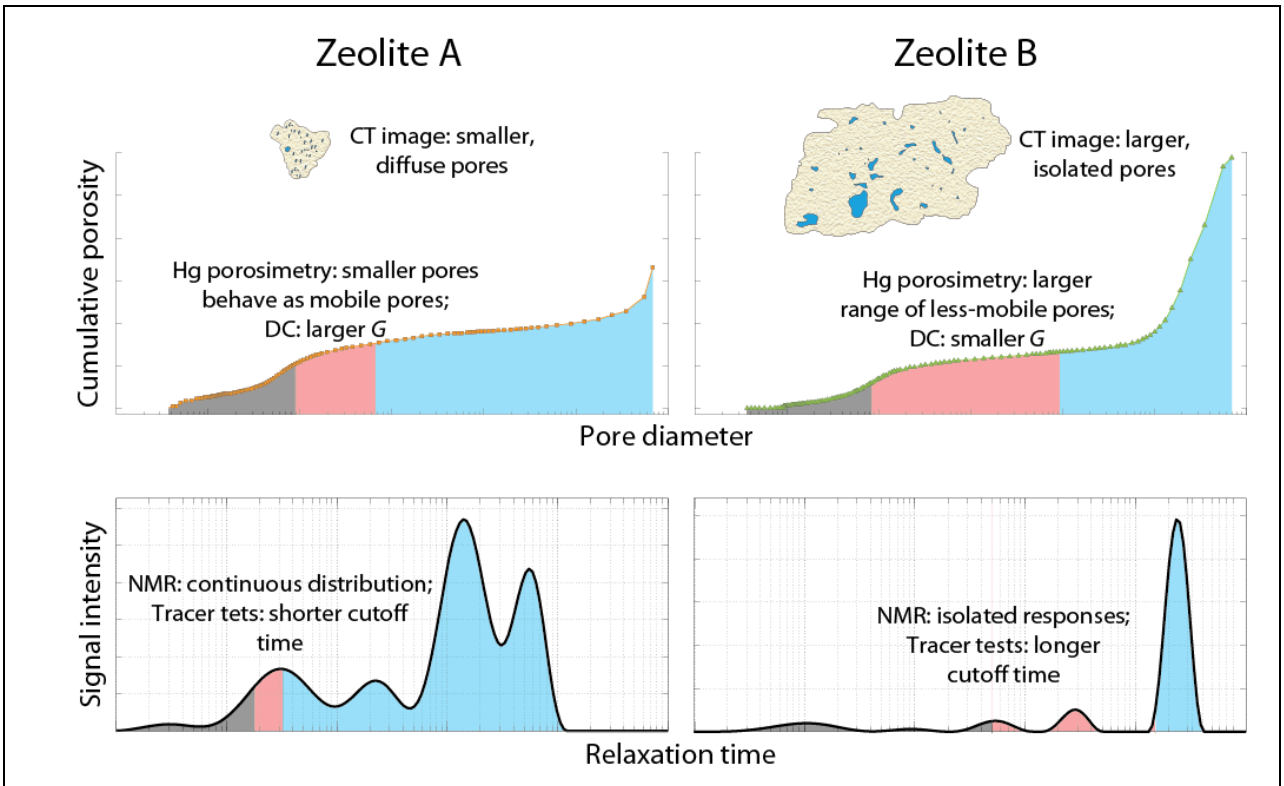

Figure 20. A simplified summary of the contrast in properties between zeolite A and zeolite B. Zeolite A has smaller and more continuous distribution of pores along with a smaller *G*; zeolite

B has larger, isolated pores and a smaller *G* [from Swanson et al., in review].

6.6. Task 3A. Field-scale Experiments at the Hanford 300 Area, Hanford, WA

Although hysteresis behavior was observed, indicating mass transfer, experimental data appear to be complicated by vadose-zone processes and simple means of analysis are not appropriate. Hanford infiltration/tracer/electrical experimental results show evidence of non-ideal behavior, including the effects of unsaturated flow and lateral flow, necessitating more complex data analysis than planned. Our experimental design aimed at developing steady-state, saturated vertical flow prior to tracer experiments. **Figure 21** presents a subset of our results, for two ports, during which a NaBr tracer was released into and flushed out of the system. Work is ongoing to analyze these data. Project PIs also plan in follow-on work to investigate signatures of mass-transfer in time-lapse electrical datasets collected by PNNL along the river corridor.

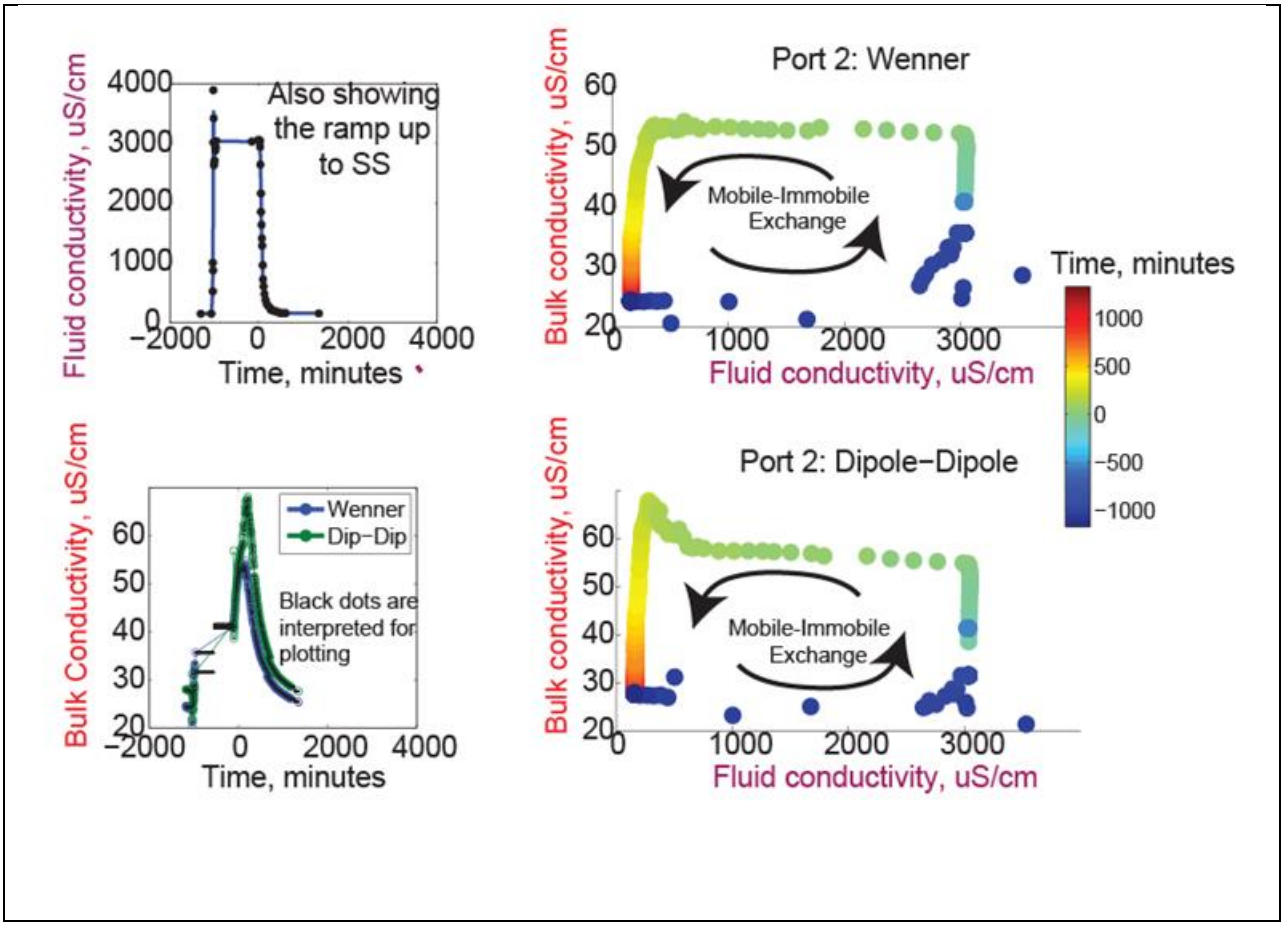

Figure 21. Data from ports 1 and 2 during NaBr release and subsequent flushing from the system.

6.6. Task 3B. Field-scale Experiments at the Naturita UMTRA Site, Naturita, CO

Changes in σ_f and σ_b through time at Naturita were assumed to result from the breakthrough of the conservative NaCl tracer, hypothetical BTCs and resulting hysteresis are shown in **Figure 22**. It should be noted that we fit the σ_b and σ_f observations directly, not a hysteresis pattern between them, because error propagation is compounded when considering ratios of measurements; hence an optimal fit to a hysteresis pattern would likely result in a poorer fit to the underlying σ_b and σ_f BTC data. With UCODE_2005 a sum of squared weighted residuals (SOSWR) objective function is minimized through the perturbation of parameter values providing the ‘‘best fit’’ between weighted observations and their simulated equivalents [*Poeter et al.*, 2005]. Before model parameters were optimized, UCODE_2005 was run in "sensitivity analysis" mode to assess possible parameter correlation. Parameters with correlation greater than 0.95 were estimated independently during initial optimization runs, then typically combined later for simultaneous convergence. The criterion for model convergence was set at the UCODE_2005 default, or less than 1% change in parameter values between iterations [*Poeter et al.*, 2005]. A non-linear confidence interval (CI) analysis was performed for the optimized parameter sets using the UCODE_2005 sensitivity analysis mode. Note that only a subset of experimental and analytical results are reported here; the interested reader is referred to Briggs et al. [2013] for additional results and sensitivity analysis.

The calibrated model closely matches the observed σ_b and σ_f characteristics at all 5 sites. We note that the σ_b vs. σ_f hysteresis patterns were not directly fit during the parameter optimization procedure, rather the calibration target was to fit the time histories (BTCs) (**Figure 22**), not the hysteresis pattern; however, the fitting process to the combined σ_f and σ_b observations effectively reproduces the general shapes and orientation of hysteresis (**Figure 23**). The notable hysteresis at $E1_{4.6}$ and $E1_{5.0}$ showed some structure during the injection limb which was primarily related to the variable tracer input concentration, and these general shapes were also well matched by the model which used the same variable input signal for all simulations. Specific mass-transfer parameter values varied strongly in space, and between the effective and local scales. The precision of parameter estimates as evaluated by the UCODE 95% confidence interval was highest for the flowpath scale immobile porosity and rate coefficient when there was notable σ_f tailing, and highest for the local scale immobile porosity and rate coefficient when hysteresis was observed.

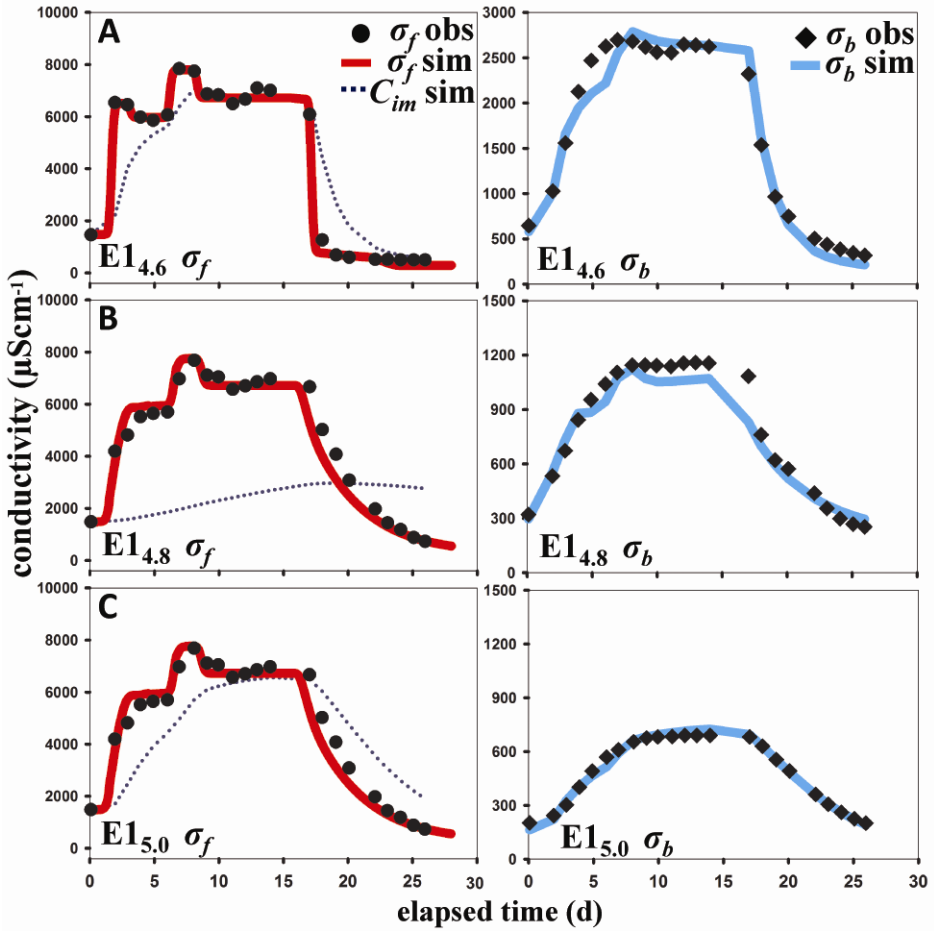

Figure 22. Fluid and bulk conductivity observations and optimized simulations are shown in respective columns, with the lettered rows corresponding to profile locations: (A) $E1_{4.6}$, (B) $E1_{4.8}$, and (C) $E1_{5.0}$.

The major findings of this part of the study are: (1) Both σ_b and σ_f observations were closely matched by regression modeling using UCODE_2005 and a multi-scale DDMT model, resulting in generally high parameter sensitivity; (2) Strong variability in mass transfer was observed in space and along the same flowpath with α spanning two orders of magnitude; (3) Hysteresis pattern structure was reproduced well in all cases even though these patterns were not explicitly fit during the parameter optimization process, (4) As indicated in previous work, greater hysteresis separation between the injection and flush limbs of BTCs yielded greater local-scale mass-transfer and higher sensitivity of the related parameters, but σ_b observations were still useful to determining local porosity and optimizing effective parameters in cases of little hysteresis; and (5) The method's "window of detection" of local-scale mass transfer can be increased using longer tracer injections to include very slow local mass-transfer processes, which

may influence long-term solute retention and release, and experimental design can be evaluated with a Eulerian based local Damköhler number.

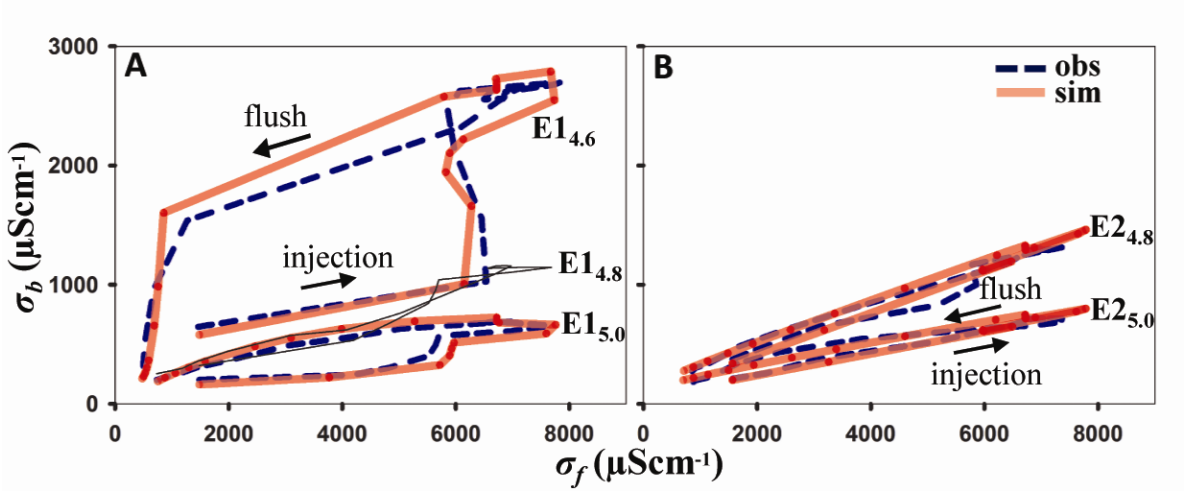

Figure 23. Hysteresis patterns between σ_b and σ_f, simulated and observed, along the (A) E1 profile that showed prominent hysteresis separation ($E1_{4.8}$ which did not have strong hysteresis as the solid black line); and (B) E2 profile which showed minimal hysteresis separation. Although hysteresis patterns were not explicitly fit during parameter optimization their structure was well simulated in all cases.

The ability to characterize spatially variable mass-transfer parameters at the field scale is a substantial advance. For the first time, we demonstrated that local processes are not well represented by flowpath-scale information. Given the combination of tracer and geoelectrical data collected during an ionic tracer test, it is possible to discriminate between the effects of upgradient-flowpath and local mass transfer. Improved estimation of immobile porosity distribution should facilitate more accurate estimates of the volume of immobile contaminant present in the field. Additionally, our approach provides information for parameterization of field-scale multi-rate mass-transfer models where the rate distribution is directly informed by measurements of the true local-scale mass transfer.

7. Products

Products from work performed under this grant span (1) methods development under Task 1 [Keery et al., 2012], (2) laboratory work including DC electrical monitoring of tracer experiments, CR, and NMR [Swanson et al., 2012, in review] under Task 2; and (3) analysis of field experimental data [Briggs et al., 2013] under Task 3. In addition, several of our PIs drew on

material from this grant in contributing to review papers on time-lapse electrical monitoring [Singha et al., in review] and work assessing the use of 'geophysical tracers' [Singha et al., 2011]. Work is ongoing to bring to publication work on pore-scale modeling [Day-Lewis et al., in prep], simple, analytical approaches to analyzing time-lapse electrical data for mass-transfer [Briggs et al., in prep], and the feasibility of using electrical methods to estimate the operation of parameters under multirate mass transfer [Swanson and Singha, in prep]. Grant products are summarized in **Table 2**.

Table 2. Major products of Grant DE-SC0001773.

Reference	Significance
(1) Briggs, M.A., Day-Lewis, F.D., Ong, J.B., Lane, J.W., Jr., (in prep), Analytical Parameter Inference for Dual-Domain Mass Transfer Based on Electrical Hysteresis, for submission to Water Resources Research.	• Presents simple, analytical approaches to estimate mass-transfer parameters from time series of bulk and fluid conductivity • Presents analysis of synthetic data; laboratory data; and field experimental data from Naturita, CO.
(2) Day-Lewis, F.D., Linde, N., Haggerty, R.D., Singha, K., (in prep), Pore-Network Simulation to Evaluate the Electrical Signature of Dual-Domain Mass Transfer, for submission to Water Resources Research.	• Presents pore-network modeling approach to simulate the electrical signature of mass transfer in time-lapse electrical data • Investigates the averaging behavior of bulk conductivity in dual-domain media
(3) Swanson, R, and Singha, K. (in prep), Temporal Moment Estimates for Dual-Domain Mass Transfer Parameters within a Multirate Mass Transfer Framework, for submission to Water Resources Research.	• Identifies the worth of incorporating electrical geophysical measurements to solute tracer tests under multirate mass transfer conditions
(4) Swanson, R., Binley, A., Keating, K., France, S., Osterman, G., Day-Lewis, F., and Singha, K., (submitted) Anomalous Solute Transport in Saturated Porous Media: Linking Transport Model Parameters to Electrical and Nuclear Magnetic Resonance Properties, 2014, in review, submitted to Water	• Compares laboratory DC, NMR, and CR data for media exhibiting dual-domain mass transfer • Evaluates CR and NMR signatures of mass transfer

Resources Research.	
(5) Singha, K., Day-Lewis, F.D., Johnson, T.C., and Slater, L.D., (2014, in review), Advances in interpretation of subsurface processes with time-lapse electrical imaging, submitted to Hydrologic Processes.	• Reviews application of time-lapse electrical methods (DC and CR) to understand transport processes relevant to hydrology
(6) Briggs, M. A., F. D. Day-Lewis, J. B. T. Ong, G. P. Curtis, and J. W. Lane (2013), Simultaneous estimation of local-scale and flow path-scale dual-domain mass transfer parameters using geoelectrical monitoring, Water Resour. Res., 49, 1–16, doi:10.1002/wrcr.20397.	• Presents field-experimental data from Naturita, CO, in which dual-domain mass transfer is evident • Presents model calibrations for a solute-transport model, demonstrating joint inversion of geophysical and tracer data
(7) Swanson, R. D., K. Singha, F. D. Day-Lewis, A. Binley, K. Keating, and R. Haggerty (2012), Direct geoelectrical evidence of mass transfer at the laboratory scale, Water Resour. Res., 48(10), doi:10.1029/2012WR012431.	• Presents controlled laboratory experimental data showing the electrical signature of dual-domain mass transfer during column tracer experiments. • Presents parametric sweeps to estimate mass-transfer parameters and evaluate the utility of time-lapse electrical measurements to understand mass transfer
(8) Keery, J., Binley, A., Elshenawy, A., Clifford, J. (2012), Markov Chain Monte Carlo Estimation of Distributed Debye Relaxations in Spectral Induced Polarization, Geophysics, 77(2), E159-E170.	• Presents and demonstrates a new approach to analyze for CR spectra
(9) Singha, K., Li L., Day-Lewis, F.D., Regberg, A.B., (2011), Quantifying Transport Processes: Are Chemically Conservative Tracers Geophysically Conservative?, Geophysics., vol. 76, no. 1, doi: 10.1190/1.3511356.	• Reviews the use of electrical imaging to monitoring tracer experiments, and discusses the implications of dual-domain mass transfer for assumptions underlying the use of conservative tracers

Abstracts and Presentations (*student authors):

Swanson, R.*, Binley, A., Keating, K., France, S.*, Osterman, G.*, Day-Lewis, F.D., Singha, K. (2013). Anomalous Solute Transport in Saturated Porous Media: Linking Transport Model Parameters to Electrical and Nuclear Magnetic Resonance Properties. EOS Trans. AGU Fall Meet. Suppl. Abstract.

Day-Lewis, F.D.,and K. Singha (2013). Geophysical Characterization and Monitoring for Anomalous Transport. EOS Trans. AGU Fall Meet. Suppl. Abstract. *Invited*.

Singha, K., Fitzgerald, M., Swanson, R.*, Voltz, T.*, Ward, A.* (2013). Electrical Identification of Parameters Controlling the Good, the Bad and the Ugly of Solute Transport. The Symposium for the Application of Geophysics to Environmental and Engineering Problems (SAGEEP), 17-21 March, Denver, CO *Invited*.

Swanson, R.*, Singha, K., Day-Lewis, F.D., Binley, A., Keating, K., Haggerty, R. (2013). Direct Geoelectrical Evidence of Mass Transfer at the laboratory scale. The Symposium for the Application of Geophysics to Environmental and Engineering Problems (SAGEEP), 17-21 March, Denver, CO.

Swanson, R.*, Binley, A., Keating K., Haggerty, R., Day-Lewis, F.D., Singha, K. (2012). The response of complex and direct-current electrical methods within a multirate non-Fickian solute transport framework. EOS Trans. AGU 93(52) Fall Meet. Suppl. Abstract H33D-1353.

Swanson, R.*, Singha, K.., Day-Lewis, F.D., Binley, A., Haggerty, R., Clifford, J.*, Keating K. (2012). Electrical Evidence for Mass Transfer at the Lab Scale. SEG-AGU Workshop on Hydrogeophysics, Boise ID, 9-12 July 2012.

Swanson, R. D.*, Singha, K., Day-Lewis, F. D., Keating, K., Binley, A., Clifford, J.*, Haggerty, R., 2011, Direct Geoelectrical Evidence of Mass Transfer at the Lab scale [abs.], in American Geophysical Union, Fall Meeting 2011, abstract #H43E-1258.

Day-Lewis, F.D., Haggerty, R., Singha, K., Binley, A.M., Swanson, R.D.*, Clifford, J.*, Lane, J.W., Jr., Ward, A., and Johnson, T.C., 2011, Pore network simulation to develop electrical petrophysical relations in the presence of mass transfer [abs.], in American Geophysical Union, Fall Meeting, 2011, abstract #NS13A-02.

REFERENCES

Day-Lewis, F.D., Singha, K. 2008, Geoelectrical Inference of Mass Transfer Parameters Using Temporal Moments, Water Resources Research, Vol. 44, W05201,

doi:10.1029/2007WR006750, 6p.

Keery, J., Binley, A., Elshenawy, A., Clifford, J. 2012, Markov Chain Monte Carlo Estimation of Distributed Debye Relaxations in Spectral Induced Polarization, Geophysics, 77(2), E159-E170.

Singha, K., Pidlisecky, A., Day-Lewis, F.D., and Gooseff, M.N., 2008, Electrical characterization of non-Fickian transport in groundwater and hyporheic systems, Water Resources Research, 44, W00D07, doi:10.1029/2008WR007048.

Singha, K., Day-Lewis, F.D., and Lane, J.W., Jr., 2007, Geoelectrical Evidence for Bicontinuum Transport in Ground Water, Geophysical Research Letters, Vol. 34 L12401, doi:10.1029/2007GL030019,